Lithos 340–341 (2019) 152–165

Contents lists available at ScienceDirect

Lithos

journal homepage: www.elsevier.com/locate/lithos

Intermediate-mafic dikes in the East Kunlun Orogen, Northern Tibetan Plateau: A window into paleo-arc magma feeding system

Fuhao Xiong [a,b,*], Changqian Ma [b], Bing Chen [a,c], Mihai N. Ducea [d,e], Mingcai Hou [c], Shijun Ni [a,f]

[a] College of Earth Science, Chengdu University of Technology, Chengdu 610059, China
[b] State Key Laboratory of Geological Processes and Mineral Resources, China University of Geosciences, Wuhan 430074, China
[c] State Key Laboratory of Oil and Gas Reservoir Geology and Exploitation, Chengdu University of Technology, Chengdu 610059, China
[d] Department of Geosciences, University of Arizona, Tucson, AZ 85721, USA
[e] Faculty of Geology and Geophysics, University of Bucharest, Bucharest, 010041, Romania
[f] Key Laboratory of Tectonic Controls on Mineralization, Hydrocarbon Accumulation of Ministry of Natural Resources, Chengdu University of Technology, Chengdu 610059, China

ARTICLE INFO

Article history:
Received 10 January 2019
Accepted 9 May 2019
Available online 16 May 2019

Keywords:
Intermediate–mafic dikes
Geochemistry
Magma reservoir
East Kunlun Orogen
Tibetan Plateau

ABSTRACT

The contemporaneous mafic and intermediate dikes of a continental magmatic arc provide a window into the magma feeding system at depth. Here we integrate data on the elemental and Sr-Nd-Hf isotope geochemistry, petrology, mineralogy, and zircon geochronology of late Permian dikes in the East Kunlun Orogen, northern Tibetan Plateau, discuss the petrogenesis of the dikes, and reconstruct the nature and relationship of different magma reservoirs. The dikes are porphyritic diabases, lamprophyres and diorite porphyries that crystallized between 259 and 255 Ma, coeval with their host granodiorites. Geochemical and Sr-Nd-Hf isotopic data indicate the parental magma of the porphyritic diabases and lamprophyres was derived from enriched lithospheric mantle. This magma underplated the crust and underwent varying degrees of magma recharging, crustal assimilation, and fractional crystallization dominated by olivine, pyroxene, and hornblende. This evolved basaltic magmas ascended through the crust, undergoing further differentiation, and some magma entered mid-crustal reservoirs occupied by felsic crystal mushes, rejuvenating the mushes. The subsequent mixing of mafic and felsic materials formed the precursor magmas of the intermediate dikes. Our new data reveal that the magmas stagnated mainly in reservoirs at two levels, 26–32 and 9–18 km, based on hornblende barometry. The underplating, assimilation, and replenishment of basaltic magmas in the lower crust, and their eventual emplacement and differentiation in a mid-crustal reservoir, controlled the mineralogy and geochemistry of the mafic dikes, while the rejuvenation of crystal mushes, the mixing of mafic and felsic materials, and differentiation account for the compositional features of the diorite porphyries. This study shows that the trans-crustal magma feeding system, which controls the compositions of several dispersed but interconnected magma reservoirs, is the key to understanding the compositional diversity and igneous petrogenesis in continental arcs.

1. Introduction

Basaltic magma underplating in the continental crust followed by interactions with the host crust is believed to be a significant process responsible for generating compositional diversity in continental magmatic arcs (Annen et al., 2006; Ducea et al., 2015; Hildreth and Moorbath, 1988). Despite considerable research on the subject, a clear picture of the magmatic processes has not yet emerged, and there remains a lack of in-depth research on the fate of the underplated basaltic magma and how mafic magma contributes to the evolution of a felsic magma reservoir (Andrews et al., 2008; Annen and Sparks, 2002; Burgisser and Bergantz, 2011). Of particular interest, and hotly debated, is where these mafic–felsic magmas form, stagnate, and differentiate before they crystallize as intrusive or extrusive rocks (Suzuki and Nakada, 2007; Weidendorfer et al., 2014). Moreover, since continental arc magmas on average straddle the andesite-dacite compositional boundary that resemble the bulk composition of continental crust, the processes of arc magmatism are key to understanding the evolution of continental crust (Ducea et al., 2015; Taylor and McLennan, 1985). Thus, identifying the sources of magma, the evolution processes and physico-chemical conditions of magma reservoirs, and establishing the genetic relationships between basaltic and felsic magma reservoirs are of fundamental significance in understanding the arc magma system that feeds the continental crust.

Continental arcs are shaped by subduction-related magmatism, and the East Kunlun Orogenic Belt (EKOB) in the northern Tibetan Plateau is

* Corresponding author at: College of Earth Science, Chengdu University of Technology, Chengdu 610059, China.
E-mail address: xiongfuhao2014@cdut.edu.cn (F. Xiong).

https://doi.org/10.1016/j.lithos.2019.05.012
0024-4937/

a prime example. The EKOB evolved via extensive arc magmatism during the Permian and Triassic, as represented by large-scale felsic arc batholiths (Mo et al., 2007; Xiong et al., 2014; Zhang et al., 2017; Fig. 1), and these batholiths provide an excellent natural laboratory to study the magmatic arc system. Previous researchers proposed that basaltic magma underplating and associated magma mixing played a major role in the generation of these batholiths, and this interpretation was based mainly on studies of microgranular magmatic enclaves (MMEs) (e.g., Chen et al., 2017; Li et al., 2018; Xiong et al., 2014). However, the origin of MMEs remains debated, and their possible genetic mechanisms include, but are not limited to, restites (Chappell and Wyborn, 2012, and references therein), mantle-derived melts (Barbarin, 2005; Mo et al., 2007), and mafic cumulates (Flood and Shaw, 2014; Moita et al., 2015). Our inability to directly observe underplated basaltic magmas means that the nature of mantle-derived melts and the exact processes of the crust–mantle interaction remain uncertain.

In this paper, we present mineralogic, petrologic, geochronological, and geochemical data for coeval mafic–intermediate dike swarms in the EKOB to constrain their generation mechanisms and associated magma processes, and to unravel the fate of the underplated basaltic magma and its relationship to the intermediate magma.

2. Geological setting and petrography

2.1. Geological setting

The EKOB extends east–west for up to 1500 km along the northern margin of the Tibetan Plateau, and is bounded by the Qaidam block to the north and the Bayan Har terrane to the south (Fig. 1a). The EKOB is a key segment to reconstruct the Tethyan realm in East Asia and formed finally during the Paleo-Tethyan accretionary orogeny in the late Permian–Triassic (Harris et al., 1988; Mo et al., 2007; Yang et al., 2009). Extensive magmatism related to the Paleo-Tethyan orogeny took place in the EKOB (Fig. 1b), as characterized by large-scale Permian–Triassic granitoids (Chen et al., 2015; Harris et al., 1988; Mo et al., 2007; Xiong et al., 2014). Recently, numerous intermediate–mafic dike swarms were discovered in the EKOB (Hu et al., 2016; Xiong et al., 2011, 2013), and most of them intruded into the coeval granitoids.

The study area is located in the eastern section of the EKOB (Fig. 1a), ~20 km south of Balong township in Qinghai Province, NW China. The country rocks of the studied dikes consist of Paleoproterozoic metasedimentary rocks, early Paleozoic granites and late Permian granodiorites, with the latter being the most important (Fig. 1b). Zircon U-Pb dating of the host granodiorites yields crystallization ages of 261–252 Ma (Xiong et al., 2012; Zhang et al., 2012), corresponding to the peak period of construction of the magmatic arc in the EKOB (Chen et al., 2015; Ding et al., 2015; Li et al., 2018; Xiong et al., 2014; Zhang et al., 2012; Zhang et al., 2017). The dikes in the Permian granitoids are subvertical and trend E–W, parallel to the central Kunlun fault system (Fig. 1b). The dikes are 0.5 to 5.0 m thick (Fig. 2a) and do not present any evidence of ductile deformation, but they commonly curve and occasionally show sharp contacts with the host pluton (Fig. 2a and b). Some mafic dikes are cut by back-veining from the host granodiorite (Fig. 2a), and some intermediate dikes contain small amounts of angular or harbor-shaped xenoliths of the host granodiorite (Fig. 2c). These features, together with the absence of thermal contact metamorphism in the host granodiorites, are characteristic of synplutonic dikes (Barbarin, 2005).

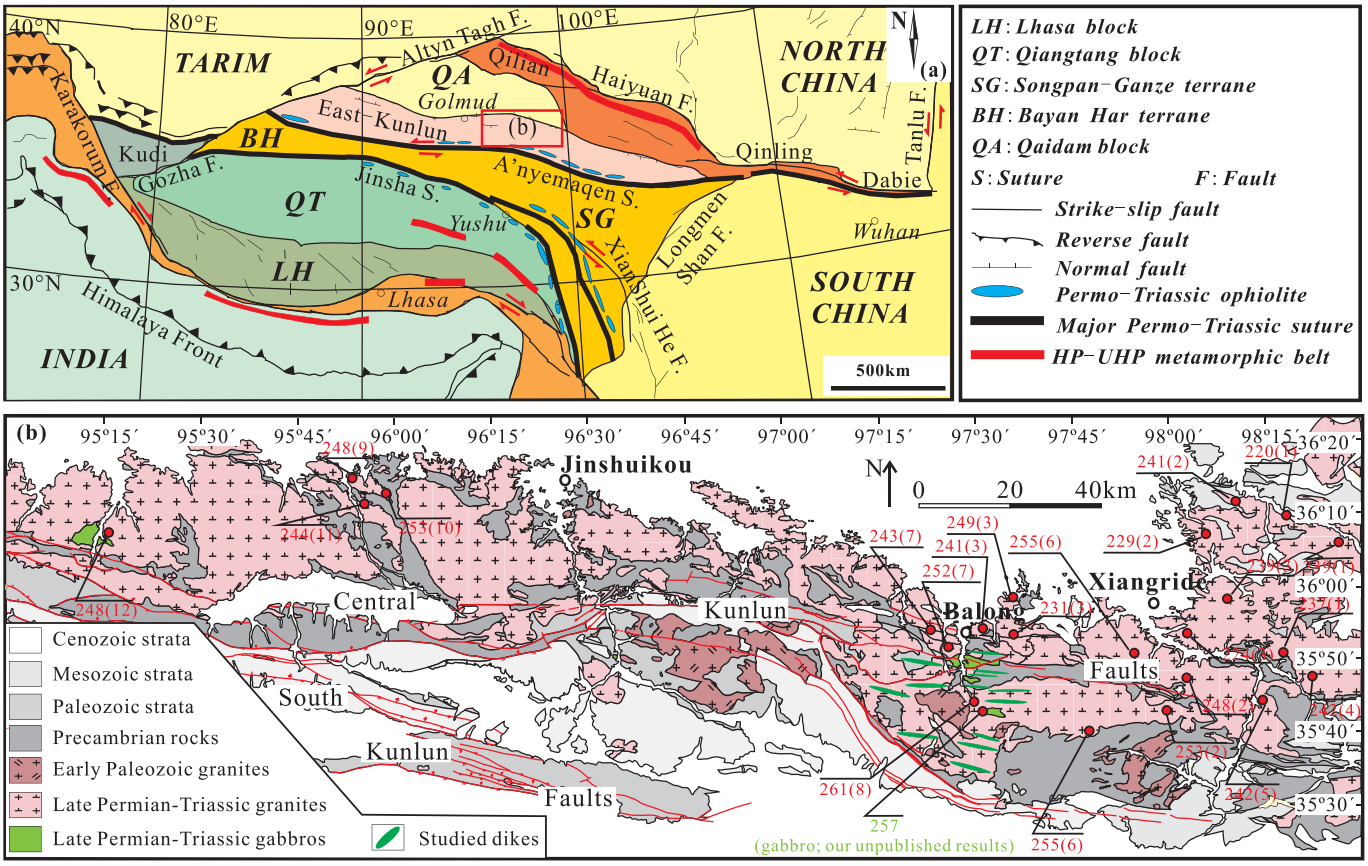

Fig. 1. (a) Tectonic outline of the Tibetan Plateau showing its major tectonic units (after Roger et al., 2008); (b) Simplified geological map of East Kunlun orogen showing the distribution of the granitic plutons and the studied dikes (after Xiong et al., 2014). Data sources for zircon U-Pb ages are as follows: 1-Shao et al. (2017); 2-Chen et al. (2015); 3-Xiong et al. (2014); 4-Chen et al. (2017); 5-Liu et al. (2004); 6-Li et al. (2018); 7-Zhang et al. (2012); 8-Xiong et al. (2012); 9-Ding et al. (2015); 10-Zhang et al. (2017); 11-Ding et al. (2014); 12-Xiong et al. (2011).

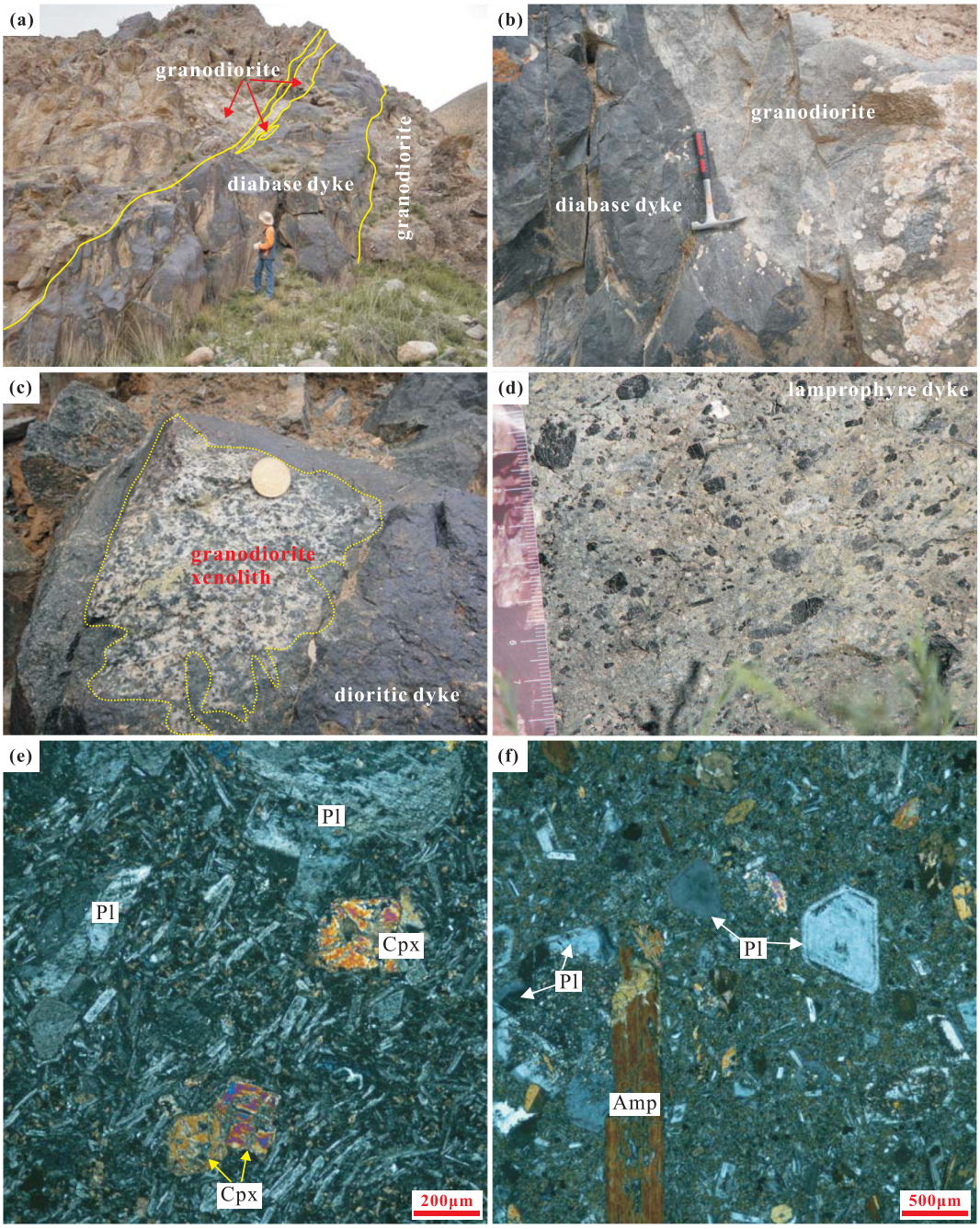

Fig. 2. (a-d) Field photographs of the studied dikes in the EKOB and (e-f) photomicrographs of representative samples. (a) Granodiorite is the host of, and back-vein in the porphyritic diabase; (b) Contact between the porphyritic diabase and host granodiorite; (c) Granodiorite xenolith in diorite porphyry; (d) Lamprophyre with abundant amphibole phenocrysts; (e) Porphyritic texture of porphyritic diabase with Cpx and Pl phenocrysts; (f) Porphyritic texture of diorite porphyry with Amp and Pl phenocrysts. Cpx-clinopyroxene, Amp-amphibole, Pl-plagioclase.

2.2. Sampling and petrography

Twenty-two representative samples were collected from fresh portions of different dikes, and four samples were collected for dating (Fig. 1b). According to their petrographic characteristics, the samples can be classified as lamprophyre, porphyritic diabase and diorite porphyry. Representative photomicrographs of the studied dikes are shown in Fig. 2.

All the dikes are massive, of fine to medium grain size, and dark gray or gray–green in color. The lamprophyres are characterized by a fine-grained porphyritic texture with phenocrysts of euhedral amphibole (15–20 vol%) and a small amount of pyroxene (Fig. 2d). The groundmass of the lamprophyres is fine-grained and made up of amphibole (30–35 vol%), plagioclase (25–30 vol%), pyroxene (5–10 vol%), and biotite (2–5 vol%). The porphyritic diabases are porphyritic with a fine-grained matrix (Fig. 2e) of subhedral plagioclase (40–45 vol%), clinopyroxene (10–15 vol%), and euhedral amphibole (20–25 vol%), and they have phenocrysts of plagioclase (~10 vol%), pyroxene (~3 vol%), and amphibole (~5 vol%). The diorite porphyries have a typical porphyritic texture with euhedral plagioclase and amphibole phenocrysts set in a matrix of fine-grained plagioclase and amphibole (Fig. 2f). Notably, the types and contents of phenocryst in the diorite porphyries vary from sample to sample, so that some samples are rich in amphibole phenocrysts but lack plagioclase phenocrysts, while others have mainly plagioclase phenocrysts.

3. Analytical methods

3.1. U-Pb dating by LA-ICP-MS methods

Zircons were separated using conventional heavy liquid and magnetic techniques at the Langfang Regional Geological Survey, Hebei Province, China. Zircon grains were photographed with an optical microscope, and their internal structure was checked by cathodoluminescence (CL). The U-Pb dating was done by (LA-ICP-MS) at the State Key Laboratory of Geological Processes and Mineral Resources (GPMR), China University of Geosciences, Wuhan. Laser sampling was performed using a GeolasPro laser ablation system that consists of a COMPexPro 102 ArF excimer laser (wavelength of 193 nm) and a MicroLas optical system. An Agilent 7500a ICP-MS instrument was used to acquire ion-signal intensities. The spot size, frequency and energy of the laser were set to 32 μm, 6 Hz and ~60 mJ, respectively, in this study. Zircon 91,500 was used as the external standard for U-Pb dating, and was analyzed twice every 5 analyses. Concordia diagrams and weighted mean calculations were made using Isoplot/Ex_ver3 (Ludwig, 2003), and data were processed by *ICPMSDataCal* (Liu et al., 2010). Detailed operating conditions for the laser ablation system and the ICP-MS instrument and data reduction are the same as described by Liu et al. (2010).

3.2. Major elemental and trace elemental analyses

Major element contents of minerals were determined at GPMR laboratory, Wuhan, using a JEOL-JXA-8100 electron microprobe analyzer (EMPA) equipped with four WDS spectrometers. The samples were first coated with a thin conductive carbon film prior to analysis. During the analysis, an accelerating voltage of 15 kV and a beam current of 20 nA were used to a 10 μm spot on the mineral surface. Precision for mineral composition analysis was calculated from counting statistics and was generally better than ±1% for measurements of >10 wt%, and better than ±5% for contents of >0.5 wt%. Detailed operating conditions for the EPMA system and data correction procedure are the same as described by Duan and Jiang (2017).

Whole rock samples were crushed in a corundum jaw crusher (to 60 mesh). About 60 g was powdered in an agate ring mill to <200 mesh for whole rock geochemistry analysis. The major-element analysis was conducted by standard X-ray fluorescence (XRF) methods, which was carried out on a Shimadzu Sequential 1800 spectrometer at the GPMR laboratory, Wuhan. Precision is better than 4% and accuracy is better than 3% for major elements. The detailed techniques for analysis of major elements are described by Ma et al. (2012). Trace elements were analyzed with an Agilent 7500a ICP-MS at GPMR laboratory, Wuhan. The samples were digested by HF + HNO_3 in Teflon bombs. Analyses of USGS standards (AGV-2, BHVO-2, BCR-2 and RGM-2) indicate accuracy better than 5–10% for most trace elements. The detailed sample-digesting procedure of ICP-MS analyses for trace elements is the same as described by Liu et al. (2008).

3.3. Sr-Nd isotope analyses

Bulk-rock Sr and Nd isotopic ratios were determined on a Finnigan Triton thermal ionization mass spectrometer at the GPMR laboratory, Wuhan. Details on the experimental procedures and analytical precision have been described by Gao et al. (2004). Total procedural blanks were < 50 pg for Sm and Nd, as well as <1 ng for Rb and Sr. The measured $^{87}Sr/^{86}Sr$ and $^{143}Nd/^{144}Nd$ ratios were normalized to the natural $^{86}Sr/^{88}Sr$ of 0.1194 and $^{146}Nd/^{144}Nd$ of 0.7219, respectively. Analyses of standards during the period of analysis are as follows: NBS987 yielded $^{87}Sr/^{86}Sr$ ratio of 0.710236 ± 16 (2σ), La Jolla yielded $^{143}Nd/^{144}Nd$ ratio of 0.511862 ± 5 (2σ).

3.4. In situ zircon Hf isotope analyses

In-situ Hf isotope analyses of zircon were conducted on the dated zircon grains using a Neptune Plus MC-ICP-MS (Thermo Fisher Scientific, Germany) in combination with a Geolas 2005 laser ablation system (Lambda Physik, Göttingen, Germany) that was hosted at the GPMR laboratory, Wuhan. All data were acquired on zircon in single spot ablation mode at a spot size of 44 μm. Each measurement consisted of 20 s of acquisition of the background signal followed by 50 s of ablation signal acquisition. Off-line selection and integration of analytical signals were performed using *ICPMSDataCal* (Liu et al., 2010). Zircon standards 91,500 and GJ-1 were used to check instrument reliability and stability. Detailed operating conditions for the laser ablation system, the MC-ICP-MS instrument and analytical method are the same as described by Hu et al. (2012).

4. Results

4.1. Zircon U-Pb ages

The zircon U-Pb data are presented in Supplementary Table S1 and representative CL images of analyzed crystals are shown in Fig. 3. All the zircons are transparent, colorless to pale yellow, columnar crystals without inclusions. All samples contain two groups of zircons, with group 1 zircons showing clear magmatic zoning and group 2 zircons showing rounded xenocrystic cores (Fig. 3). All the zircons in group 1 are euhedral to subhedral, but their internal textures vary, which might indicate different origins (Corfu et al., 2003). The group 1 zircons from the lamprophyre sample show homogeneous, faint broad zoning, and they have length/width ratios of 2–4 (Fig. 3a), the group 1 zircons from the diorite porphyry samples show typical oscillatory zoning (Fig. 3b and d), and those from the porphyritic diabase show sector zoning with length/width ratios of about 1 (Fig. 3c).

The group 1 zircons from lamprophyre sample 10NM56-2 have high Th and U contents (Th = 353–1189 ppm, U = 450–1201 ppm; Supplementary Table S1) and high ratios of Th/U (0.52–0.99), confirming their magmatic origin (Hoskin and Schaltegger, 2003). Seventeen spots were analyzed on these zircons, and they gave concordant $^{206}Pb/^{238}U$ dates ranging from 260 to 251 Ma and a weighted mean date of 256.3 ± 1.2 Ma (MSWD = 0.86, errors are 1σ), which is identical to their intercept date of 256.1 ± 1.4 Ma (Fig. 3a). On the other hand, two spots on the xenocrystic cores of group 2 zircons showed low Th and U contents (Th = 134–248 ppm, U = 151–298 ppm) and old concordant $^{206}Pb/^{238}U$ dates (403–387 Ma) that record Devonian thermal events in the EKOB.

Two samples of diorite porphyry were used for zircon dating (samples 10NM58-2 and 11BL11-7). The xenocrystic cores in group 2 zircons yielded $^{206}Pb/^{238}U$ dates of 928 to 342 Ma, whereas the group 1 zircons gave young $^{206}Pb/^{238}U$ dates similar to those of the lamprophyre. The magmatic zircons from samples 10NM58-2 and 11BL11-7 yielded weighted mean $^{206}Pb/^{238}U$ dates of 255.1 ± 1.9 and 255.2 ± 2.5 Ma, respectively (Fig. 3b and d), which are consistent with their intercept $^{206}Pb/^{238}U$ dates, suggesting the diorite porphyries were emplaced during the late Permian.

The sector zoned zircons from the porphyritic diabase specimen have high contents of Th and U (Th = 446–1571 ppm, U = 794–2532 ppm) and high ratios of Th/U (0.22–1.12). These zircons gave $^{206}Pb/^{238}U$ dates ranging from 263 to 255 Ma (Fig. 3c) and a weighted mean date of 259.2 ± 1.8 Ma (MSWD = 0.29, 1σ), which is within error of the intercept date of 257.7 ± 3.0 Ma. The xenocrystic zircon cores have similar Th and U contents to the sector zoned zircons, but old $^{206}Pb/^{238}U$ dates ranging from 893 to 697 Ma (Fig. 3c).

The geochronological data show, therefore, that the studied dikes of lamprophyre, porphyritic diabase, and diorite porphyry have identical crystallization ages, which suggests that coeval mafic and intermediate magmatism took place at ca. 259–255 Ma.

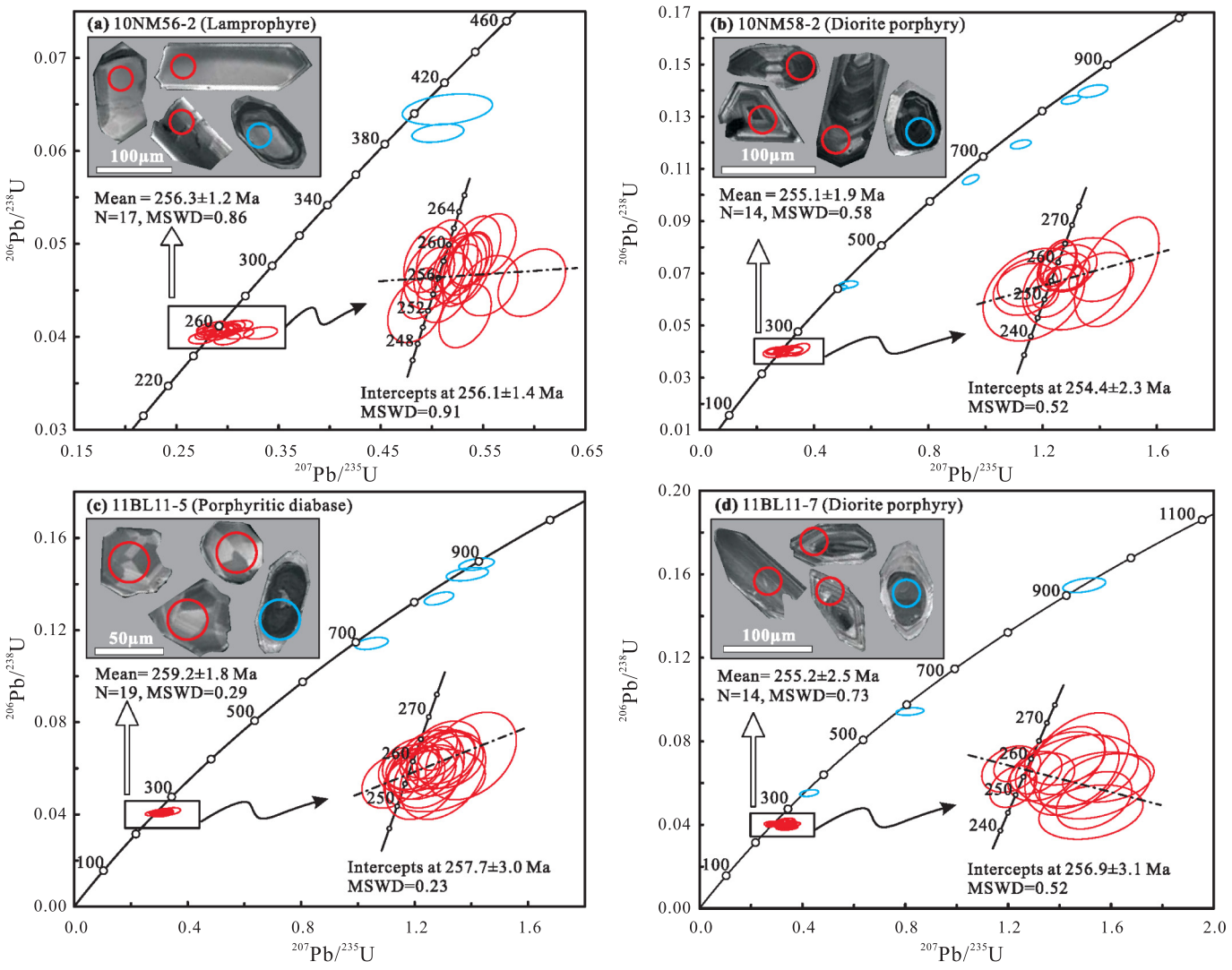

Fig. 3. Representative CL images of zircons and U-Pb concordia diagrams for the studied dikes. (a) Lamprophyre dike (10NM56-2); (b) Diorite porphyry dike (10NM58-2); (c) Porphyritic diabase dike (11BL11-5); (d) Diorite porphyry dike (11BL11-7).

4.2. Mineral compositions

Since plagioclase, pyroxene, and amphibole dominate the mineral assemblages of the studied dikes, a study of their compositions and textural characteristics can be used to assess the nature of the magma and its evolutionary changes. Thus, we studied these minerals to investigate the nature of the open- or closed-system processes that affected the magma.

4.2.1. Plagioclase

The analytical data for the plagioclases are listed in Supplementary Table S2, and their An–Ab–Or compositions are shown on Fig. 4. All the plagioclases in the lamprophyres are present only in the matrix and they lack any zoning. Their anorthite contents range from 42 to 49 (andesine) (Fig. 4a). In contrast, the plagioclases in the porphyritic diabase and diorite porphyries have complex textures and compositional variations (Fig. 4). The porphyritic diabases are heterogeneous, as shown by the matrix plagioclases, which can be divided into two contrasting groups of anorthite–bytownite (An_{85-90}) and labradorite (An_{68-69}). Moreover, the plagioclase phenocrysts in the porphyritic diabases show either normal zoning or no zoning. The plagioclase phenocrysts with normal zoning have CaO- and Al_2O_3-rich cores with An contents of 80–82, and diverse compositions of An = 69–71 in the rims (Fig. 4b), while the unzoned phenocrysts have similar compositions to the rims of the normally zoned plagioclases (An = 68–73; Fig. 4a). Thus, there are two groups of plagioclase phenocrysts in the porphyritic diabases with An contents of 80–82 (group 1) and 68–73 (group 2).

Most plagioclase phenocrysts in the diorite porphyries show reverse zoning with anorthite contents of 34–50 in the cores (andesine) and 57–69 in the rims (labradorite) (Fig. 4d). The plagioclases in the matrix (An = 59–62) and a few unzoned phenocrysts (An = 61–63) are relatively homogeneous and have compositions that are similar to those of the rims of the reverse-zoned phenocrysts.

4.2.2. Amphibole

The compositions of the analyzed amphiboles are listed in Supplementary Table S3. The matrix amphibole and amphibole phenocrysts in the lamprophyres have similar compositions (Fig. 5a and b) that are close to pargasite with high contents of K_2O (0.74–0.91 wt%) and FeO^T (14.75–17.54 wt%), low contents of Al_2O_3 (10.07–11.44 wt%) and MgO (9.95–11.27 wt%), and low values of $Mg^{\#}$ (52–57, $Mg^{\#}$ = 100*Mg/(Mg + Fe) in mole proportions, assuming all the iron is Fe^{2+}).

However, the amphibole phenocrysts in the porphyritic diabases show normal zoning with significant variations in their major elements

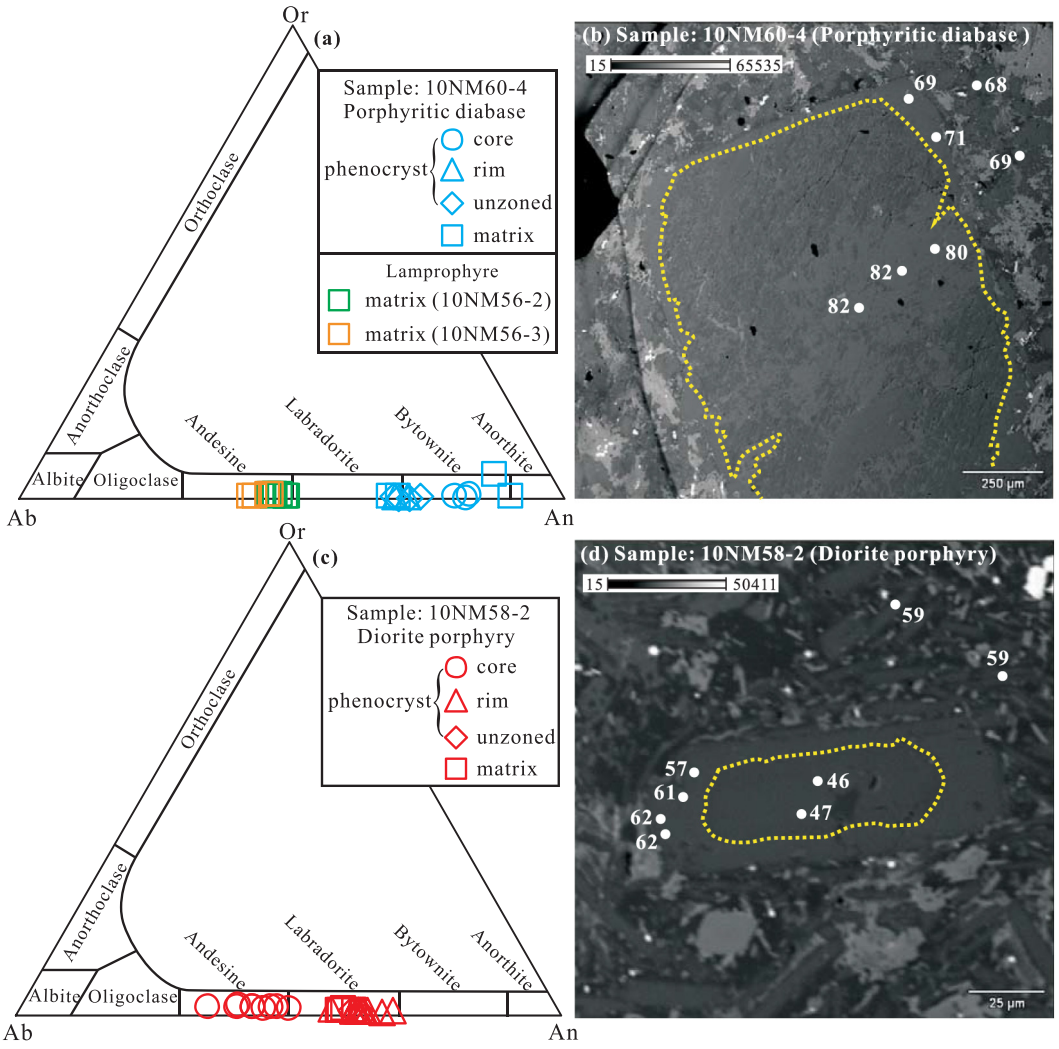

Fig. 4. (a, c) Chemical compositions and (b, d) backscattered electronic images (BSE) of plagioclases from the studied dikes in EKOB.

(Fig. 5d). For example, the cores can be classified as magnesiohastingsite with $Mg^{\#}$ values of 58–72 and high contents of TiO_2 (2.54–2.72 wt%), MgO (11.13–14.00 wt%), and Na_2O (2.23–2.51 wt%), while the rims have low contents of TiO_2 (0.28–2.60 wt%), MgO (8.21–12.24 wt%), and Na_2O (1.13–1.84 wt%), and can be divided into either ferrohornblende ($Mg^{\#}$ = 54–64) or tschermakite ($Mg^{\#}$ = 42–48).

In contrast, the amphibole phenocrysts in the diorite porphyries show reverse zoning (Table S3; Fig. 5). Most of the phenocryst cores show varied compositions ranging from tschermakite to ferrotschermakite with $Mg^{\#}$ values of 46–55 (Fig. 5), but the rims can all be classified as tschermakite with much higher values of $Mg^{\#}$ (60–62), and higher contents of TiO_2 (2.30–2.70 wt%) and MgO (12.20–12.98 wt%). Some unzoned amphibole phenocrysts can be classified as magnesiohastingsite with moderate $Mg^{\#}$ values (~58) and high contents of CaO (11.20–11.54 wt%), Na_2O (2.17–2.28 wt%), and K_2O (0.47–0.52 wt%).

4.2.3. Pyroxene

The major element compositions for the pyroxenes are listed in Supplementary Table S4. As illustrated on Fig. 6, all the investigated pyroxenes phenocrysts are diopside to augite in composition. Although these phenocrysts are homogeneous and lack zoning (Fig. 2e), there are compositional differences between the pyroxenes of the lamprophyres and the porphyritic diabases. The phenocrysts in the lamprophyres have a relatively narrow compositional range (Wo45-39 En30-29 Fs30-25) with $Mg^{\#}$ values ranging from 51 to 55, while those in the porphyritic diabases have a relatively wide compositional range (Wo50-43 En37-34 Fs21-14) with $Mg^{\#}$ values of 64 to 74 (Table S4).

4.3. Whole-rock geochemistry

4.3.1. Major elements

Whole-rock major- and trace-element analytical results are presented in Supplementary Table S5. The concentrations of the major elements, in weight percent, have been recalculated from the determined values to 100% on a volatile-free basis. The lamprophyres and porphyritic diabases show gabbroic compositions, characterized by a narrow range of SiO_2 (49.08–55.30 wt%), high contents of total Fe as FeO^T (8.36–10.02 wt%) and CaO (7.80–11.02 wt%), and moderate contents of MgO (3.78–8.83 wt%) and values of $Mg^{\#}$ (41–61). On Fig. 7 they fall on a trend from the calc-alkaline to shoshonitic fields with high contents of Na_2O and K_2O.

The diorite porphyries have compositions identical to andesite, and they have higher contents of SiO_2 and Na_2O, lower contents of TiO_2, FeO^T, MgO and CaO, and lower values of $Mg^{\#}$ (21–45) than the mafic dikes (Table S5). Their high contents of SiO_2 (57.42–63.64 wt%) and

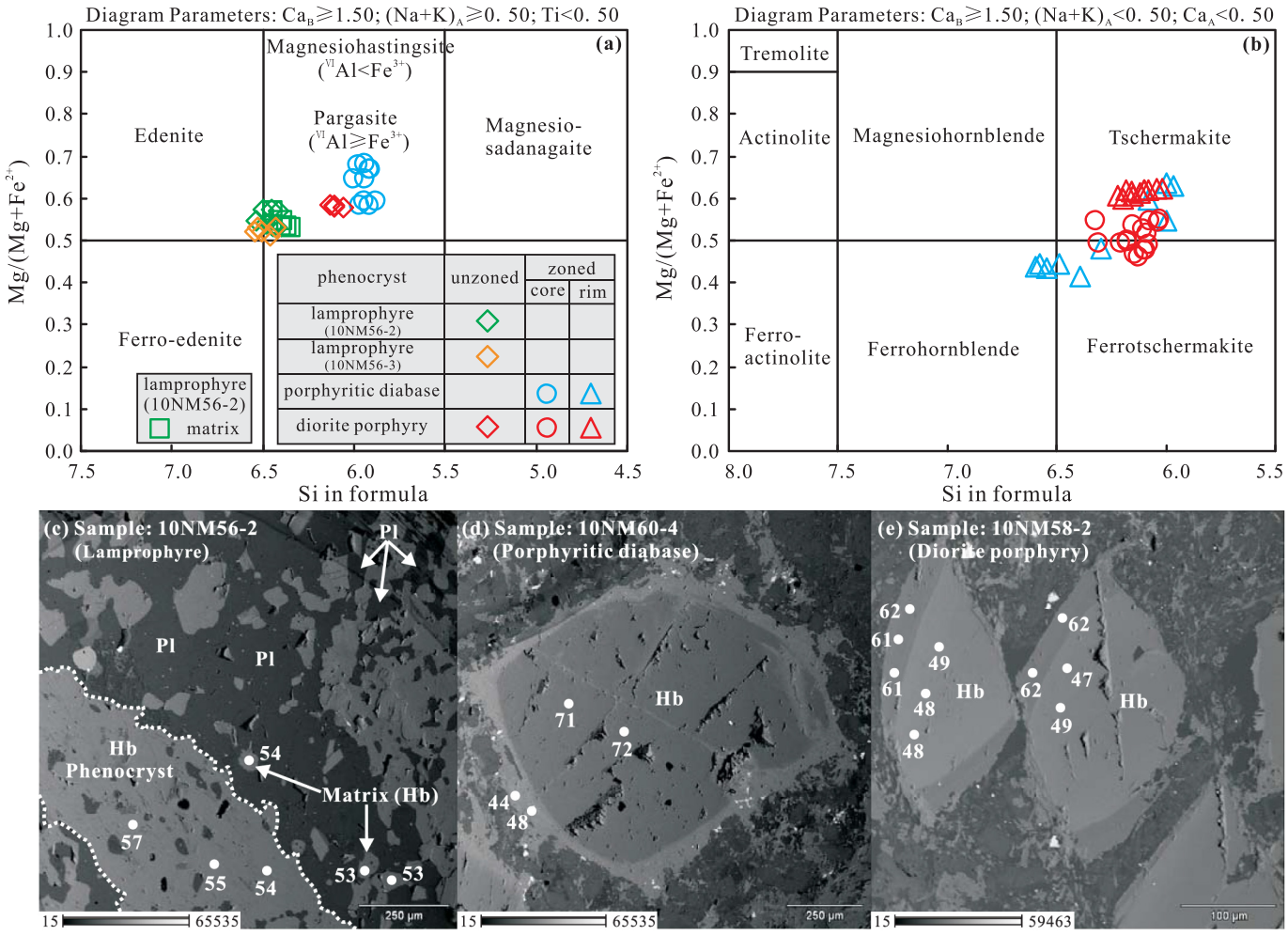

Fig. 5. (a-b) Composition and classification (Leake et al., 1997) for the amphibole phenocrysts from the studied dikes in East Kunlun; (c) BSE image for the lamprophyre (10NM56-2), showing the amphibole phenocryst without zoning texture; (d) BSE image for the porphyritic diabase (10NM60-4), showing the normal zoned amphibole phenocryst; (e) BSE image for the diorite porphyry (10NM58-2), showing the reverse zoned amphibole phenocryst.

K_2O + Na_2O (5.03–6.59 wt%) resemble those of typical (high-K) calc-alkaline diorites (Fig. 7).

4.3.2. Trace elements

The porphyritic diabases and lamprophyres have similar rare-earth element (REE) compositions (∑REEs = 83–130 and 113–138 ppm, respectively), and they exhibit slight enrichments of light rare earth elements (LREEs; $(La/Yb)_N$ = 4.42–7.52 and 6.15–9.37, respectively) and flat patterns of the heavy rare-earth elements (HREEs; Fig. 8a and c), except for sample 11BL11-9 (∑REEs = 196 ppm, $(La/Yb)_N$ = 11.67). In contrast, the diorite porphyries have higher total REE contents (∑REEs = 134–205 ppm), and they are much more enriched in LREEs relative to the HREEs ($(La/Yb)_N$ = 6.86–18.16). The mafic and intermediate dikes show either no Eu anomaly (Eu/Eu^* = 0.87–1.01) or a slight negative Eu anomaly (Eu/Eu^* = 0.70–1.02) (Fig. 8).

The primitive mantle-normalized trace element variation diagrams (Fig. 8b and d) show that the mafic dikes are strongly enriched in large ion lithophile elements (LILEs; e.g., Rb, Ba, Th, U, and Pb) and depleted in P, Ti, and high field-strength elements (HFSEs; e.g., Ta, Nb, Zr, and Hf). Compared with the mafic dikes, the intermediate dikes are much more enriched in LILEs as well as Zr and Hf (Fig. 8f).

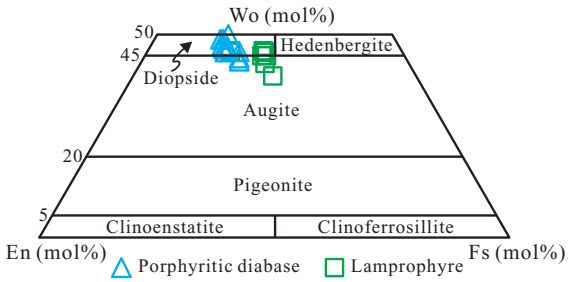

Fig. 6. Ternary En-Wo-Fs chemical classification of clinopyroxene phenocrysts from the porphyritic diabase and lamprophyre in EKOB.

4.4. Sr-Nd-Hf isotopes

The bulk-rock Sr-Nd and zircon Lu-Hf isotope data are presented in Supplementary Table S6 and S7, respectively. All isotopic ratios were calculated using the crystallization age of the corresponding dike. The mafic dikes have weakly enriched Sr-Nd isotopic compositions (Table S6; Fig. 9a), with high initial Sr isotopic ratios ($(^{87}Sr/^{86}Sr)_i$ = 0.7090–0.7117) and moderate $\varepsilon_{Nd}(t)$ values (−6.37 to −3.70), while the diorite porphyries have relatively high initial Sr isotopic ratios ($(^{87}Sr/^{86}Sr)_i$ = 0.7104–0.7122) and low $\varepsilon_{Nd}(t)$ values (−7.86 to −5.98).

The zircons from the porphyritic diabase show varied Lu-Hf isotopic compositions (Table S7; Fig. 9b), with the majority showing chondrite-like isotopes ($\varepsilon_{Hf}(t)$ = 0.39 to 3.19). On the other hand, the zircons from the lamprophyre have relatively homogenous Lu-Hf isotopes, characterized by moderate initial $^{176}Hf/^{177}Hf$ ratios (0.282533–0.282637) and weakly enriched $\varepsilon_{Hf}(t)$ values (−2.79 to 0.91). With the exception of

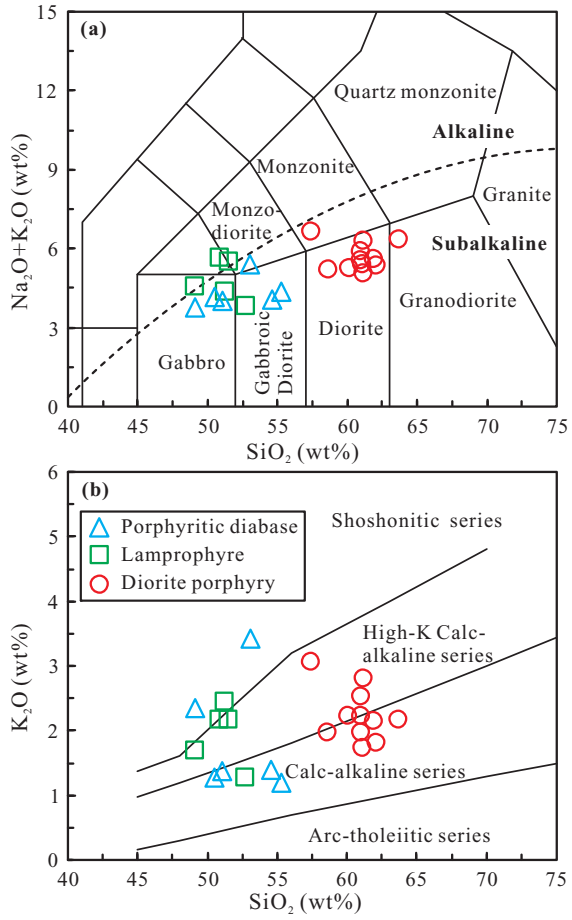

Fig. 7. Chemical classifications of the studied dikes in EKOB. (a) TAS classification diagram (Middlemost, 1994); (b) K_2O vs SiO_2 diagram (Peccerillo and Taylor, 1976).

one spot with a high initial $^{176}Hf/^{177}Hf$ ratio (0.282748) and a depleted $\varepsilon_{Hf}(t)$ value (4.82), all the zircons in the diorite porphyry have the same Lu-Hf isotopic compositions as those from the lamprophyre, with initial $^{176}Hf/^{177}Hf$ ratios of 0.282537–0.282620 and enriched $\varepsilon_{Hf}(t)$ values of −2.63 to 0.29.

5. Discussion

5.1. Crystallization conditions in the magma reservoirs

Our samples of calcic amphibole and clinopyroxene phenocrysts and/or xenocrysts preserve a record of the compositional variations in the magma feeding system during crystal growth, and this could provide critical petrogenetic information on the evolution of the magma reservoir (Ginibre et al., 2007; Streck, 2008). The amphibole-related thermobarometric equation proposed by Ridolfi et al. (2010); Ridolfi and Renzulli (2011) was applied to calculate the crystallization conditions of our dike samples (Ridolfi et al., 2010; Ridolfi and Renzulli, 2011), because it is applicable to a wider range of conditions (550–1130 °C and <2200 MPa for calc-alkaline magmas) and has lower uncertainties (T ± 23.5 °C, P ± 11.5%) than other amphibole thermobarometers such as the Al-in-hornblende geobarometer of Anderson et al. (2008, and references therein). Our results show that the amphibole phenocrysts in the lamprophyres crystallized at mid-crustal levels (276–320 MPa and 893–926 °C for sample 10NM56-2, and 248–287 MPa and 884–905 °C for sample 10NM56-3; Fig. 10), indicating its parental magma was emplaced at a depth of 9–12 km (assuming a crustal density of 2.7 g/cm^3). Interestingly, the zoned amphibole phenocrysts in the porphyritic diabases show different P-T conditions, i.e., the magnesiohastingsite cores ($Mg^{\#}$ = 58–72) and ferrohornblende rims ($Mg^{\#}$ = 54–64) exhibit high P-T values (701–856 MPa and 980–1041 °C), equating to a depth of 26–32 km, whereas the tschermakite rims ($Mg^{\#}$ = 42–48) gave much lower P–T values (P = 232–337 MPa and T = 834–899 °C). These differences suggest that the amphibole phenocrysts in the porphyritic diabases were successively overgrown in different magma reservoirs at two different depths of 26–32 and 9–12 km.

The rims and cores of the zoned amphiboles in the diorite porphyries exhibit similar crystallization pressures (330–470 MPa and 338–468 MPa, respectively), but the rims (923–965 °C) show slightly higher temperatures than the cores (881–954 °C; Fig. 10). The unzoned amphibole phenocrysts ($Mg^{\#}$ = 53–58) exhibit identical crystallization conditions to the rims, with pressures of 414–481 MPa and temperatures of 952–961 °C. Altogether, these pressures and temperatures indicate that the cores of amphibole phenocrysts ($Mg^{\#}$ = 46–55) in the diorite porphyries crystallized in a mid-crustal magma reservoir (12–18 km depth) at relatively low temperatures, and that the cores were then overgrown by the high-$Mg^{\#}$ rims ($Mg^{\#}$ = 60–62) during the subsequent injection of high-temperature magma into the reservoir.

To gain a better understanding of the T–P conditions of the magmatic processes, clinopyroxene thermobarometry was also used to constrain the conditions of crystallization. The clinopyroxene thermobarometer with the highest precision and smallest systematic error is that of Putirka et al. (2003), which we applied to our samples. Our calculations indicate that the P–T conditions of crystallization for the clinopyroxene phenocrysts from the porphyritic diabases (572–880 MPa and 1113–1159 °C) were higher than for those from the lamprophyres (211–400 MPa and 1054–1071 °C). This further confirms that the magma reservoir of the lamprophyre accumulated at mid-crustal levels (8–15 km) compared with the lower-crustal reservoir for its porphyritic diabase precursor (22–33 km), and these results are consistent with the results from amphibole thermobarometry (9–12 km and 26–32 km, respectively).

Our previous study of the coeval host granodioritic pluton revealed that it crystallized at pressures of 290–418 MPa, which equate to a depth of 11–16 km (Xiong et al., 2012), identical to the depths indicated for the diorite porphyry and lamprophyre dikes. Altogether, our study shows that magma reservoirs related to the dikes and the host granodiorite stagnated at the two levels of 26–32 and 9–18 km.

5.2. Origin and evolution of the mafic magmas

5.2.1. Magma source

Our samples of the mafic dikes (porphyritic diabase and lamprophyre) have relatively low SiO_2 contents (49.08–55.30 wt%), high MgO contents (3.78–8.83 wt%), $Mg^{\#}$ values of 41–61, no cumulate textures (Fig. 2), and chondrite-like or weakly depleted Hf isotopes, all of which suggests they were derived from a mantle source rather than the early accumulation of mafic minerals in a crustal melt (Lee et al., 2006; Rapp et al., 2003). Their high initial $^{87}Sr/^{86}Sr$ ratios (0.7090–0.7117), negative $\varepsilon_{Nd}(t)$ values (−6.37 to −3.70), and chondrite-like Hf isotopes ($\varepsilon_{Hf}(t)$ = −4.21 to 3.19 for the porphyritic diabase and −2.79 to 0.91 for the lamprophyre) are consistent with derivation from an enriched mantle source rather than a depleted asthenospheric mantle source (e.g., MORB and OIB; Fig. 9a).

This hypothesis is supported by their arc-related geochemical features, such as the marked enrichment in LILEs and depletion in HFSEs, which implies an enrichment mechanism that was related to subducted components. The relative enrichments of Rb, Th, Ta, and Ba (Fig. 8), and the obvious depletion in Yb and Y, as well as the high Th/Yb and Ba/La ratios (Fig. 11), indicate that mantle below a continental arc, enriched in fluid, could account for these geochemical features. In fact, the presence of abundant amphiboles in the mafic dikes also implies a high-H_2O (fluid-saturated) magma source (Figs. 2 and 5). Recent studies have shown that the volatile contents (e.g., H_2O_{melt}) of calc-alkaline

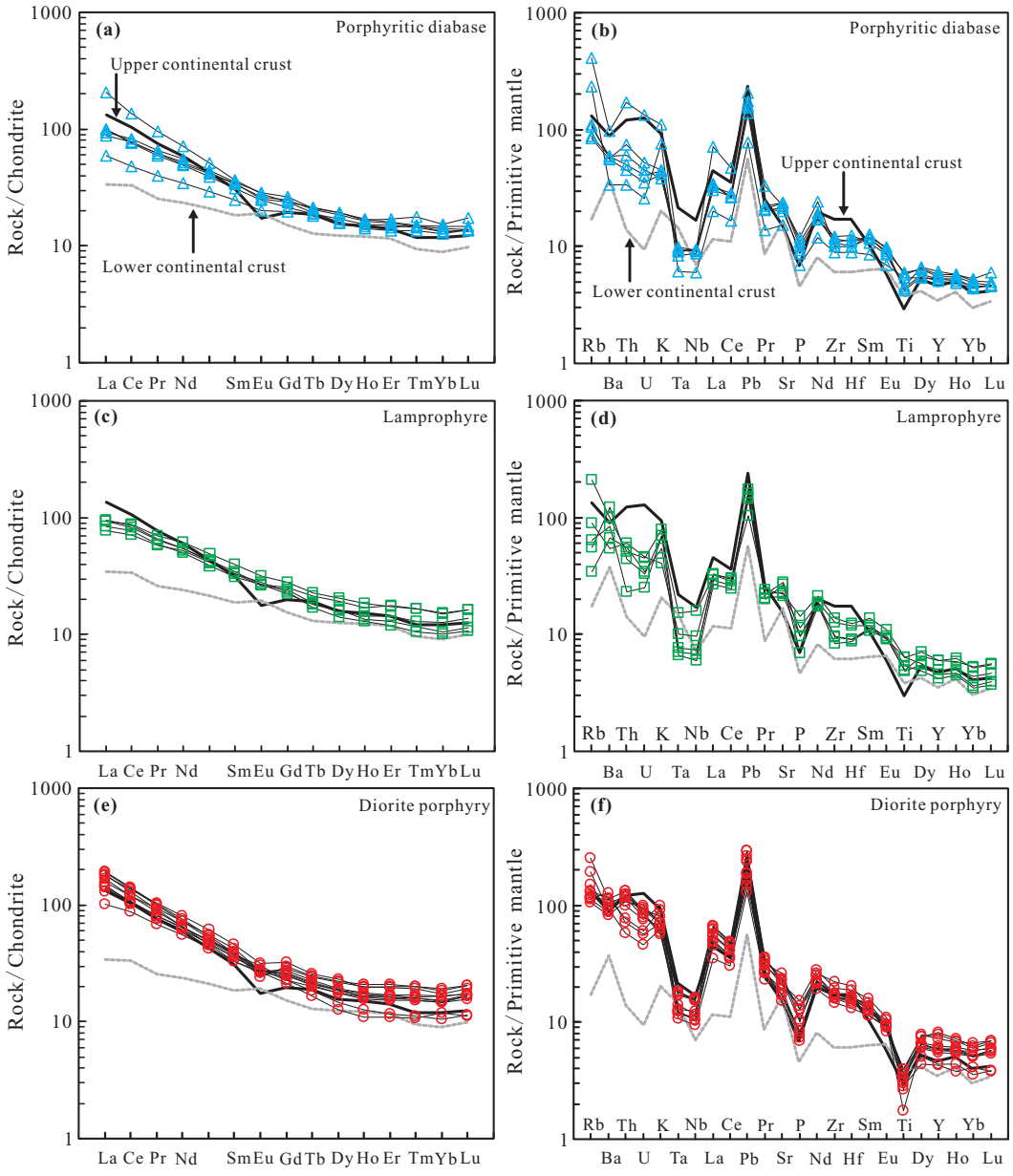

Fig. 8. Chondrite-normalized REE patterns and Primitive mantle-normalized trace element spider diagrams for the studied dikes in EKOB. (a-b) Porphyritic diabases; (c-d) Lamprophyres; (e-f) Diorite porphyries. Chondrite REE abundances are after Taylor and McLennan (1985), trace element abundances for the primitive mantle are after Sun and McDonough (1989).

melts can be related roughly to the calcic amphibole compositions and positively correlated with pressure, in agreement with most solubility models (Ridolfi and Renzulli, 2011, and references therein). Thus, the empirical method of Ridolfi and Renzulli (2011) was applied to estimate the H_2O content of the mafic magma, and the results reveal high H_2O contents (6.4–7.1 wt% for lamprophyre and 8.2–9.5 wt% for porphyritic diabase). Thus, the mineralogical, geochemical, and isotopic data for the mafic dikes all suggest derivation from an enriched lithospheric mantle source that had been metasomatized by subduction-related fluids.

5.2.2. Magmatic processes: contamination, mixing and fractionation?

It is inevitable that continental contamination or magma mixing would occur within the trans-crustal mafic magma system (Andrews et al., 2008; Annen et al., 2006; Weidendorfer et al., 2014). The REE and trace element compositions of our mafic dike samples resemble those of the upper continental crust (Fig. 8a–d), which could imply a crustal component in the genesis of the mafic dikes. Their low Nb/U ratios (2.3–21) (cf. Nb/U = 9.0–21 for crust and 34–50 for mantle) and high Th/Yb ratios (0.76–6.72) (cf. Th/Yb = 0.80–5.25 for crust and 0.04–0.25 for primitive mantle and MORB; Sun and McDonough, 1989) also indicate the contribution of crustal contamination or magma mixing. This inference is further supported by the positive correlation between $Mg^{\#}$ and εNd(t), and the negative correlation between $Mg^{\#}$ and $(^{87}Sr/^{86}Sr)_i$ (Fig. 12k and l) as well as the presence of xenocrystic zircons in these mafic dikes (Fig. 3). However, magma mixing can be ruled out, as mixing with crustal melts would have left a mark on the phenocrysts, such as the regrowth of plagioclase to form zoning with low-An rims. As shown on Fig. 4, the plagioclase phenocrysts in the porphyritic diabases do show zoning, but their rims have high contents of CaO (An = 69–71), which differs from the phenocryst cores in the coeval diorite porphyries (An = 34–50) and host granodiorites (An = 30–44; Xiong et al., 2012). Thus, crustal contamination is the most likely way in which the compositions of the mafic dike magmas were changed, and variable degrees of contamination could account for the differences in the elemental and isotopic contents of the porphyritic diabases and lamprophyres (Figs. 9 and 11).

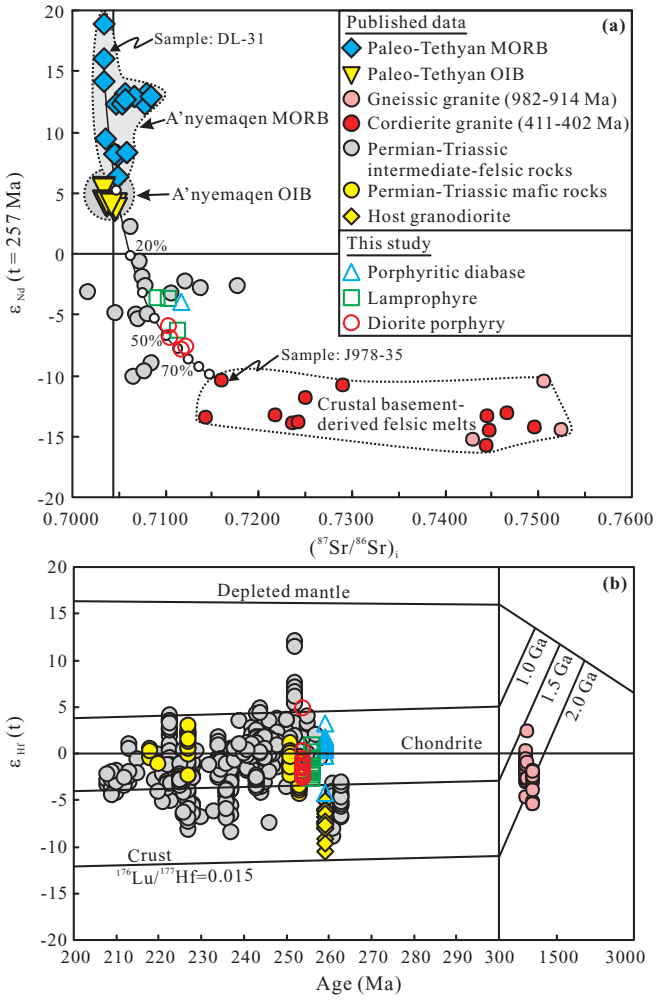

Fig. 9. Sr-Nd-Hf isotopic compositions for the studied dikes in EKOB. (a) Plots of whole-rocks ($^{87}Sr/^{86}Sr)_i$ vs εNd(t). (b) Plots of εHf(t) vs U-Pb ages for zircons. Data sources are as follows: MORB (e.g., sample DL-31: $^{87}Sr/^{86}Sr = 0.7036$, $^{143}Nd/^{144}Nd = 0.513559$, Sr = 134 ppm, Nd = 3.70 ppm) and OIB in the south Kunlun A'nyemaqen Paleo-Tethyan suture zone are from Bian et al. (2004) and Guo et al. (2007); Gneissic granites are from Chen et al. (2007) and He et al. (2016, 2018); Cordierite granites (e.g., sample J978-35: $^{87}Sr/^{86}Sr = 0.7246$, $^{143}Nd/^{144}Nd = 0.511974$, Sr = 159 ppm, Nd = 23.1 ppm) are from Ba et al. (2012) and Yu (2005); Permian-Triassic intermediate-felsic rocks are from Chen et al. (2015), Ding et al. (2014), Li et al. (2018), Xia et al. (2015), Xiong et al. (2014), and references therein; Permian-Triassic mafic rocks are from Hu et al. (2016), Liu et al. (2017) and Xiong et al. (2011, 2013); Host granodiorites are from Xiong et al. (2012).

The low values of $Mg^{\#}$ (41–61) and the low contents of Cr (6.86–295 ppm) and Ni (4.29–48.4 ppm) (Table S5; Fig. 12h–j) suggest fractional crystallization also played a significant role in the formation of the mafic dike magmas. Furthermore, $Mg^{\#}$ shows linear correlations with SiO_2, TiO_2, Al_2O_3, FeO^T, MgO, CaO, Cr, Co, and Ni for the porphyritic diabases and the lamprophyres (Fig. 12a–j), indicating that olivine, pyroxene, and hornblende dominated the fractionation. This conclusion is also consistent with the results of fractionation simulation (Fig. 12), in which we assumed that the most mafic sample represents the initial composition (sample 11BL11-2, $Mg^{\#} = 61$, Cr = 295 ppm). Fractionation of the observed mineral assemblage from hydrous mafic precursors (H_2O = 6.4–9.5 wt%) also reasonably explains the very high Al_2O_3 contents of the mafic dikes (16.69–20.27 wt%), similar to the low-MgO high-alumina basalts and basaltic andesites derived from the fractionation of hydrous (≥4 wt% H_2O) mafic magmas that pond at moderate (>6 km) crustal levels (Grove et al., 2003; Sisson and Grove, 1993).

5.3. Generation mechanism for the intermediate dikes

Compared with the mafic dikes, the petrogenesis of the intermediate dikes (i.e., the diorite porphyries) is much more complex. There are several possible mechanisms for the generation of intermediate magmas in an orogenic belt, including: (1) dehydration melting of subducted oceanic crust (Defant and Drummond, 1990; Kay, 1978), (2) slab-related melt–mantle interactions (Goss et al., 2013; Tatsumi, 2001), (3) partial melting of continental crust (Annen et al., 2006; Petford and Atherton, 1996), (4) differentiation crystallization of mantle-derived mafic magmas (Annen and Sparks, 2002; Grove et al., 2003), and (5) open-system magmatic processes, such as mixing or mingling between felsic and mafic magmas (Hildreth and Moorbath, 1988; Weidendorfer et al., 2014). The key to identifying the possible mechanism is clarifying the source affinity of the intermediate magma and its relationship to the coeval mantle-derived magma. Considering our new data on Sr–Nd–Hf isotopes and the bulk-rock and mineral chemistries, we propose that the intermediate dikes were generated from the mixing of mafic and felsic magmas in an open-system. The main evidence in support of this proposal is summarized below.

Firstly, the diorite porphyries are characterized by low contents of MgO (0.82–3.03 wt%) and values of $Mg^{\#}$ (21–45), moderate contents of Sr (323–552 ppm), and high contents of Y (19.5–37.2 ppm) and Yb (1.77–3.26 ppm), which contrasts with the adakitic-like geochemistry of melts generated by dehydration melting of subducted oceanic crust (Defant and Drummond, 1990; Kay, 1978) and the chemistry of high-Mg andesites related to melt–mantle interactions (Goss et al., 2013; Tatsumi, 2001). Moreover, the enriched Sr-Nd-Hf isotopic

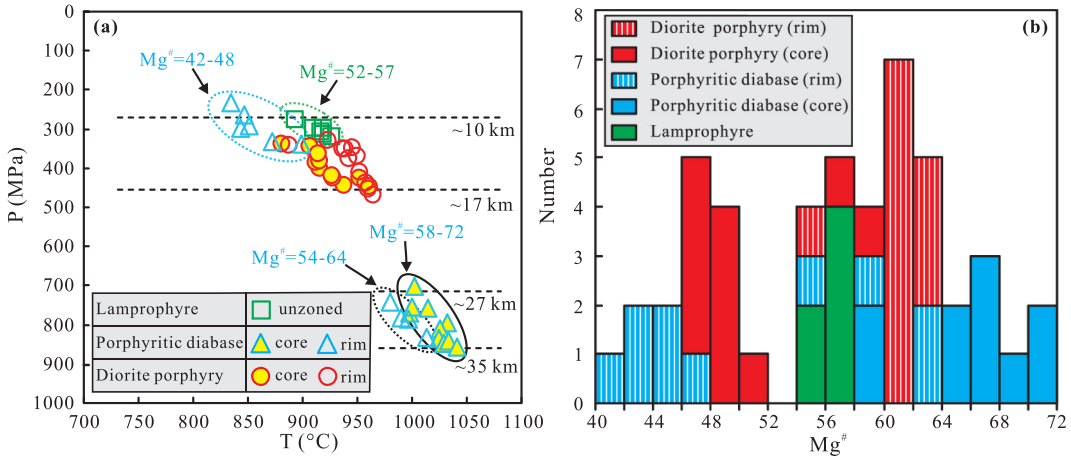

Fig. 10. (a) Calculated pressure and temperature values, and (b) the histogram of $Mg^{\#}$ for the amphibole phenocrysts from the studied dikes in EKOB.

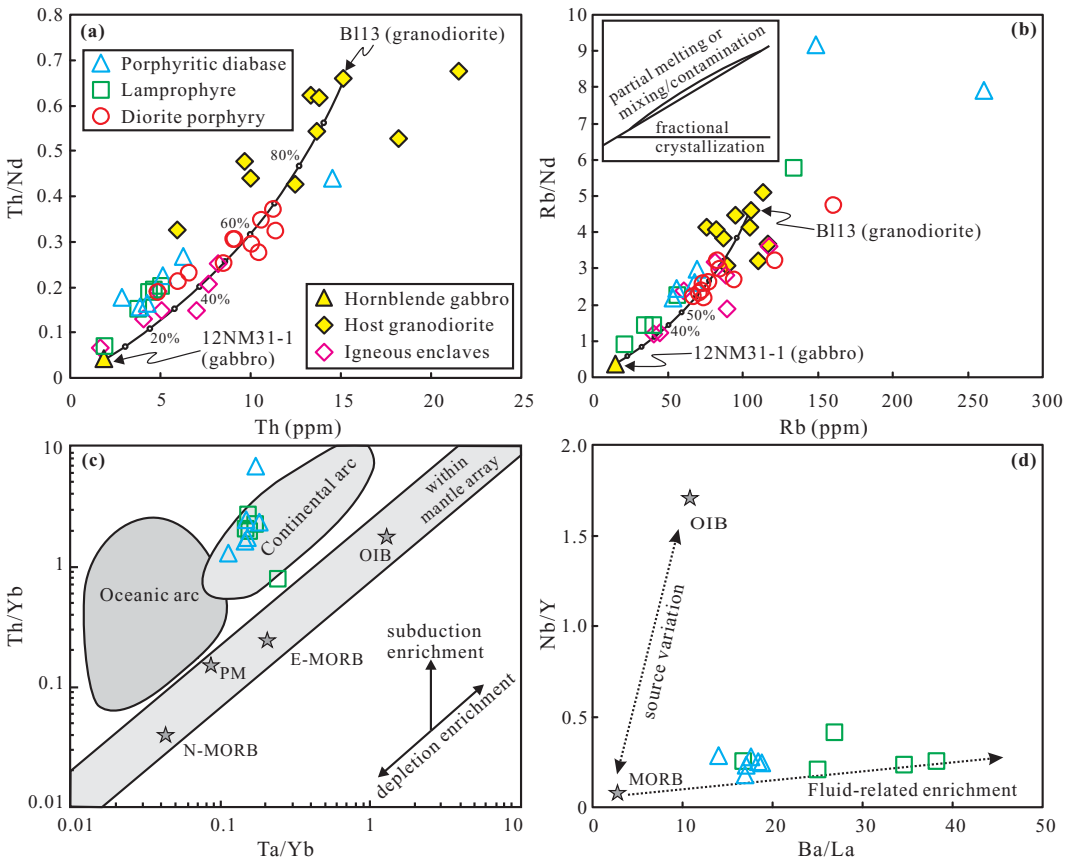

Fig. 11. Binary trace elemental diagrams for the studied dikes in EKOB. (a-b) Th/Nd vs. Th and Rb/Nd vs. Rb diagrams showing the magma mixing for the studied dikes (Schiano et al., 2010). The host granodiorites and enclaves are from Xiong et al. (2012) and Zhang et al. (2012), the hornblende gabbro is our unpublished results; (c) Th/Yb vs. Ta/Yb diagram showing the influence of subduction (Pearce, 2008); (d) Nb/Y vs. Ba/La diagram showing the fluid-related enrichment. The data for OIB, (*E*- or N-) MORB, PM are from Sun and McDonough (1989).

compositions are not only quite different from the isotopic compositions of Tethyan-related OIB and MORB-type basalts in the EKOB (Fig. 9a), but they plot far from the fields of pure crust-derived rocks (Fig. 9a and b; Chen et al., 2007; He et al., 2018), which further precludes the above two mechanisms as well as the model of simple anatexis of continental crust.

Secondly, although less profound, the diorite porphyries display much more enriched Nd-Hf isotopic signatures ($\varepsilon_{Nd}(t) = -7.86$ to -5.98 and $\varepsilon_{Hf}(t) = -2.63$ to 0.29) than the most mafic dikes (e.g., the porphyritic diabases have $\varepsilon_{Nd}(t) = -3.88$, $\varepsilon_{Hf}(t) = 0.39$ to 3.19 for most zircons). This characteristic, as well as the different evolutionary trends of Sr-Nd isotopes with increasing degrees of evolution (Fig. 12k and l), contradicts the differentiation model (Annen and Sparks, 2002; Grove et al., 2003), and this conclusion is further supported by the obvious variations in incompatible trace elements ratios (Fig. 11; Schiano et al., 2010).

In fact, the identical crystallization ages of the mafic–intermediate dikes and their host granodiorites (261–252 Ma; Xiong et al., 2012; Zhang et al., 2012), their sharp contacts without any metamorphic margins, and the presence of irregular xenoliths of the host granodiorite in the diorite porphyries (Fig. 2c) all indicate that the host felsic pluton had not completely solidified prior to the intrusion of the mafic–intermediate dikes, which makes magma mixing a possibility. Moreover, the reverse zoning of phenocrysts in the diorite porphyries records abundant information about the magmatic processes. For example, some plagioclase phenocrysts in the diorite porphyries have core–rim textures with average An values of 46–47 (cores) and 57–62 (rims) (Fig. 4d), while most amphibole phenocrysts have $Mg^{\#}$ values of 47–49 (cores) and 61–62 (rims) (Fig. 5e). These abrupt compositional changes are most likely to have been produced by magma mixing in an open system.

We evaluated this mixing hypothesis with two-component mixing model, using the spatially and temporally associated gabbro (Fig. 1b; ca. 257 Ma, $SiO_2 = 44.31$ wt%; our unpublished results) and the host granodiorite (ca. 261 Ma, $SiO_2 = 64.24$ wt%; Xiong et al., 2012) as end-member compositions. As shown by the plots of Th/Nd versus Th and Rb/Nd versus Rb (Fig. 11a and b), a mixing model of 50%–70% felsic magma and 30%–50% mafic magma could reproduce the measured trace element compositions of the diorite porphyries. This is in good agreement with the Sr-Nd isotopic mixing modeling of pure mantle-derived magmas and crustal end-members (Fig. 9a). Such a model of mixing is similar to that proposed for the genesis of the MMEs in the EKOB (Xiong et al., 2012; Zhang et al., 2012), further confirming their origin by the mixing of crust- and mantle-derived magmas.

5.4. Implications for the continental arc magma feeding system

The above observations on the petrogenesis of the dikes and their crystallization conditions show that processes of crustal contamination, magma underplating, and the subsequent mixing of mafic and felsic magmas and their differentiation controlled the compositions of the mafic and felsic magma reservoirs at two different levels in the crust. Further studies on the crystals suggest that the replenishment of basaltic magma and the rejuvenation of felsic crystal mushes were also crucial to the magma system.

The plagioclase phenocrysts in the porphyritic diabases are zoned with a significant component gap between the rims (An = 69–71) and the cores (An = 80–82) (Fig. 4b), and this is not consistent with a

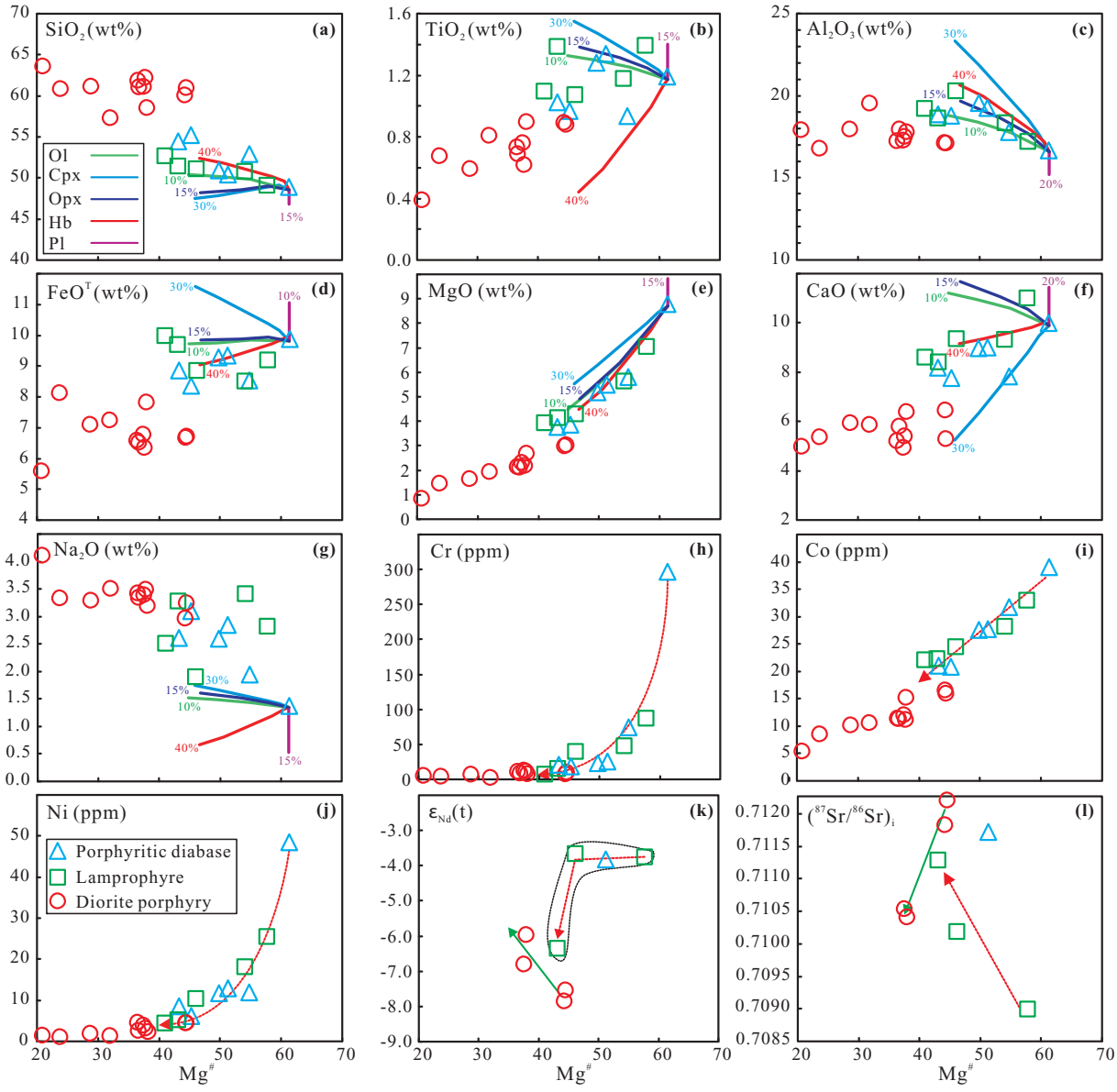

Fig. 12. (a-g) Major elemental, (h-j) trace elemental and (k-l) Sr-Nd isotopic variations with decreasing $Mg^{\#}$. The fractional curves in (a-g) are MELTS modeling results for the mafic dikes, using the most primitive sample (11BL11-2) to represent the parental magma.

fractional crystallization model, which would have produced oscillatory zoning with gradually changing components (Ginibre et al., 2007, and references therein), but is similar to the situations involving the replenishment of basaltic magma (Andrews et al., 2008; Ginibre et al., 2007). The labradorite–bytownite compositions of the phenocryst rims (An = 69–71) suggest crystallization from a basaltic rather than felsic magma (Coote and Shane, 2016; Weidendorfer et al., 2014). Some of the amphibole phenocrysts in the porphyritic diabase have a similar feature, with rims (ferrohornblende, $Mg^{\#}$ = 54–64; Table S3) exhibiting compositions that are identical to those found in basaltic magmas (Andrews et al., 2008; Streck, 2008). These features, as well as the presence of two groups of plagioclase compositions in the matrix of the porphyritic diabases ($An_{85–90}$ and $An_{68–69}$), all support the proposal that the replenishment of basaltic magma was an important process in the evolution of the magmatic system.

In the diorite porphyries, the compositions of the plagioclase matrix ($An_{59–62}$), the unzoned phenocrysts ($An_{61–63}$), and the zoned phenocryst rims ($An_{57–69}$) all fall in the range of labradorite, which contrasts with the andesine composition ($An_{34–50}$) of the phenocryst cores (Fig. 4). The same kind of reverse zoning can also be seen in some amphibole phenocrysts (Fig. 10b). Considering the presence of felsic xenoliths (Fig. 2c) and the identical crystallization depths and ages of these dikes and the host felsic pluton (Xiong et al., 2012), the reverse mineral zoning can reasonably be explained by a model involving remobilization and mixing (Fig. 13). In such a model, a mushy felsic magma, rich in andesine and low-$Mg^{\#}$ amphibole ($Mg^{\#}$ = 46–50), would have been rejuvenated by and subsequently mixed with the basaltic magma that was underplating the crust. The magma produced would have become hotter and more Ca- and Mg-rich, eventually leading to the growth of labradorite and high-$Mg^{\#}$ amphibole rims. Crystal mush remobilization and subsequent mixing are widely recognized processes in volcanic systems, as demonstrated by petrology, geophysics, and numerical modeling (Burgisser and Bergantz, 2011; Coote and Shane, 2016; Suzuki and Nakada, 2007).

Thus, combining the data on the petrography, mineralogy, and geochemistry of the studied mafic–intermediate dikes, we can reconstruct the magma feeding system as follows. (1) The parental magma of the porphyritic diabase was at first involved in the underplating of the

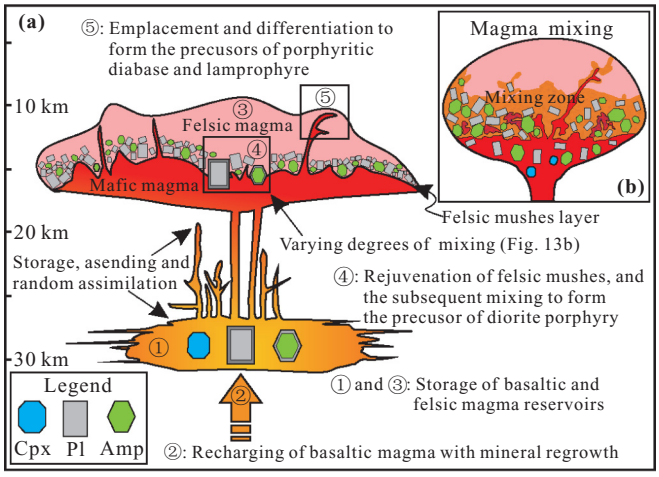

Fig. 13. (a) A hypothetic cross-section for the magma reservoirs located at two different depths, illustrating some of the major evolution processes in the magma feeding system that controlled the mineral and chemical variations of the studied dikes. (b) Magma mixing between basaltic magma and felsic mush magma.

crust. It then stagnated in a lower-crustal magma reservoir (P = 701–856 MPa, 26–32 km depth) where it was differentiated by the crystallization of clinopyroxene ($Mg^{\#}$ = 64–74, T = 1113–1159 °C), plagioclase ($An_{80–82}$), and amphibole ($Mg^{\#}$ = 58–72, T = 998–1041 °C). Meanwhile, some of the basaltic magma penetrated the lower crust and became ponded in a mid-crustal reservoir (P = 276–320 MPa), where eventually it formed the lamprophyre magma compositions through the fractional crystallization of clinopyroxene ($Mg^{\#}$ = 51–55, T = 1054–1071 °C) and amphibole ($Mg^{\#}$ = 53–57, T = 893–926 °C). (2) Recharging of the evolved basaltic magma sustained the lower magma reservoir (Fig. 13), leading to the regrowth of phenocrysts rimmed by Ca-rich plagioclase ($An_{68–73}$) and Mg-rich amphibole (ferrohornblende, $Mg^{\#}$ = 54–64) under similar P–T conditions (P = 742–831 MPa, T = 980–1013 °C). (3) At mid-crustal levels (P = 330–470 MPa), some of the evolved basaltic magma (~940 °C) ascended to the interface of a felsic crystal mush reservoir (~915 °C). Reheating by this basaltic magma would have triggered the remobilization of the crystal mush (Fig. 13), and this would have been followed by the mixing of the basaltic magma and felsic mush to form the precursor of the diorite porphyries.

6. Conclusions

A detailed petrological, geochronological, mineralogical and geochemical study of the ca. 259–255 Ma mafic–intermediate dike swarms in the EKOB provides insight into the nature of the magma feeding system and the processes involved. Geochemical and Sr–Nd–Hf isotopic data suggest that the mafic dikes were derived from an enriched lithospheric mantle that had been metasomatized by subduction-related fluids. This primary basaltic magma underplated the crust where it underwent varying degrees of magma recharging and assimilation, followed by differentiation due to the crystal fractionation of olivine, pyroxene, and hornblende. The ascent of some of this evolved mafic magma into a mid-crustal magma reservoir filled with a felsic crystal mush led to the rejuvenation of the mush and the mixing of the mafic and felsic components to form the intermediate dike magmas. We proposes that the magma feeding system involved magma underplating, replenishment, rejuvenation of felsic crystal mushes, mixing of mafic and felsic components, and differentiation, and that all these major processes, in combination, controlled the compositions of several magma reservoirs at different depths in the crust. Studying these processes in detail is key to understanding the compositional diversity and igneous petrogenesis in continental magmatic arcs.

Acknowledgments

We sincerely thank the Editor-in-Chief Prof. Xian-Hua Li and two anonymous reviewers for their constructive comments and suggestions, which substantially improved our manuscript. This study was financially supported by National Natural Science Foundation of China (No. 41602049, No. 41272079, No. 41672196), China Postdoctoral Science Foundation (No. 2015M582529) and China Scholarship Council (201708515111). Ducea acknowledges support from US National Science Foundation Grant EAR 1725002 and Romanian Executive Agency for Higher Education, Research, Development and Innovation Funding (PN-III-P4-ID-PCE-2016-0127, PN-III-P4-ID-PCCF-2016-0014).

Appendix A. Supplementary data

Supplementary data to this article can be found online at https://doi.org/10.1016/j.lithos.2019.05.012.

References

Anderson, J.L., Barth, A.P., Wooden, J.L., Mazdab, F., 2008. Thermometers and thermobarometers in granitic systems. Rev. Mineral. Geochem. 69, 121–142.
Andrews, B.J., Gardner, J.E., Housh, T.B., 2008. Repeated recharge, assimilation, and hybridization in magmas erupted from El Chichón as recorded by plagioclase and amphibole phenocrysts. J. Volcanol. Geotherm. Res. 175, 415–426.
Annen, C., Sparks, R.S.J., 2002. Effects of repetitive emplacement of basaltic intrusions on thermal evolution and melt generation in the crust. Earth Planet. Sci. Lett. 203, 937–955.
Annen, C., Blundy, J.D., Sparks, R., 2006. The genesis of intermediate and silicic magmas in deep crustal hot zones. J. Petrol. 47, 505–539.
Ba, J., Chen, N.S., Wang, Q.Y., Wang, X.Y., Zhang, L., Wang, S.Q., 2012. Nd-Sr-Pb isotopic compositions of cordierite granite on southern margin of the Qaidam block, NW China, and constraints on its petrogenesis, tectonic affinity of source region and tectonic implications. J. Earth Sci. 37, 80–92 (in Chinese with English abstract).
Barbarin, B., 2005. Mafic magmatic enclaves and mafic rocks associated with some granitoids of the Central Sierra Nevada batholith, California: nature, origin, and relations with the hosts. Lithos 80, 155–177.
Bian, Q.T., Li, D.H., Pospelov, I., Yin, L.M., Li, H.S., Zhao, D.S., Chang, C.F., Luo, X.Q., Gao, S.L., Astrakhantsev, O., Chamov, N., 2004. Age, geochemistry and tectonic setting of Buqingshan ophiolites, North Qinghai-Tibet Plateau, China. J. Asian Earth Sci. 23, 577–596.
Burgisser, A., Bergantz, G.W., 2011. A rapid mechanism to remobilize and homogenize highly crystalline magma bodies. Nature 471, 212–215.
Chappell, B.W., Wyborn, D., 2012. Origin of enclaves in S-type granites of the Lachlan Fold Belt. Lithos 154, 235–247.
Chen, N.S., Wang, X.Y., Zhang, H.F., Sun, M., Li, X.Y., Chen, Q., 2007. Geochemistry and Nd-Sr-Pb isotopic compositions of granitoids from Qaidam and Oulongbuluke microblocks, NW China: constraints on basement nature and tectonic affinity. J. Earth Sci. 32, 7–21 (in Chinese with English abstract).
Chen, X., Gehrels, G., Yin, A., Zhou, Q., Huang, P., 2015. Geochemical and Nd-Sr-Pb-O isotopic constrains on Permo-Triassic magmatism in eastern Qaidam Basin, northern Qinghai-Tibetan plateau: implications for the evolution of the Paleo-Tethys. J. Asian Earth Sci. 114, 674–692.
Chen, J., Wei, J., Fu, L., Li, H., Zhou, H., Zhao, X., Zhan, X., Tan, J., 2017. Multiple sources of the Early Mesozoic Gouli batholith, Eastern Kunlun Orogenic Belt, northern Tibetan Plateau: linking continental crustal growth with oceanic subduction. Lithos 292-293, 161–178.
Coote, A.C., Shane, P., 2016. Crystal origins and magmatic system beneath Ngauruhoe volcano (New Zealand) revealed by plagioclase textures and compositions. Lithos 260, 107–119.
Corfu, F., Hanchar, J.M., Hoskin, P.W.O., Kinny, P., 2003. Atlas of zircon textures. Rev. Mineral. Geochem. 53, 469–495.
Defant, M.J., Drummond, M.S., 1990. Derivation of some modern arc magmas by melting of young subducted lithosphere. Nature 347, 662–665.
Ding, Q., Jiang, S., Sun, F., 2014. Zircon U-Pb geochronology, geochemical and Sr-Nd-Hf isotopic compositions of the Triassic granite and diorite dikes from the Wulonggou mining area in the Eastern Kunlun Orogen, NW China: Petrogenesis and tectonic implications. Lithos 205, 266–283.
Ding, Q., Liu, F., Yan, W., 2015. Zircon U-Pb geochronology and Hf isotopic constraints on the petrogenesis of Early Triassic granites in the Wulonggou area of the Eastern Kunlun Orogen, Northwest China. Int. Geol. Rev. 57, 1735–1754.
Duan, D., Jiang, S., 2017. In situ major and trace element analysis of amphiboles in quartz monzodiorite porphyry from the Tonglvshan Cu-Fe (Au) deposit, Hubei Province, China: insights into magma evolution and related mineralization. Contrib. Mineral. Petrol. 172, 1–17.
Ducea, M.N., Saleeby, J.B., Bergantz, G., 2015. The architecture, chemistry, and evolution of continental magmatic arcs. Annu. Rev. Earth Planet. Sci. 43, 299–331.
Flood, R.H., Shaw, S.E., 2014. Microgranitoid enclaves in the felsic Looanga monzogranite, New England Batholith, Australia: pressure quench cumulates. Lithos 198, 92–102.

Gao, S., Rudnick, R.L., Yuan, H.L., Liu, X.M., Liu, Y.S., Xu, W.L., Ling, W.L., Ayers, J., Wang, X.C., Wang, Q.H., 2004. Recycling lower continental crust in the North China craton. Nature 432, 892–897.
Ginibre, C., Worner, G., Kronz, A., 2007. Crystal zoning as an archive for magma evolution. Elements 3, 261–266.
Goss, A.R., Kay, S.M., Mpodozis, C., 2013. Andean Adakite-like high-Mg andesites on the Northern Margin of the Chilean-Pampean Flat-slab (27-28.5° S) associated with frontal arc migration and fore-arc subduction erosion. J. Petrol. 54, 2193–2234.
Grove, T.L., Elkins-Tanton, L.T., Parman, S.W., Chatterjee, N., Müntener, O., Gaetani, G.A., 2003. Fractional crystallization and mantle-melting controls on calc-alkaline differentiation trends. Contrib. Mineral. Petrol. 145, 515–533.
Guo, A.L., Zhang, G.W., Sun, Y.G., Cheng, S.Y., Qiang, J., 2007. Sr-Nd-Pb isotopic geochemistry of late-Paleozoic mafic volcanic rocks in the surrounding areas of the Gonghe basin, Qinghai province and geological implications. Acta Petrol. Sin. 23, 747–754 (in Chinese with English abstract).
Harris, N.B.W., Xu, R.H., Lewis, C.L., Hawkesworth, C.J., Zhang, Y.Q., 1988. Isotope geochemistry of the 1985 Tibet geotraverse, Lhasa to Golmud. Philos. Trans. R. Soc. London, Ser. A 327, 263–285.
He, D., Dong, Y., Zhang, F., Yang, Z., Sun, S., Cheng, B., Zhou, B., Liu, X., 2016. The 1.0Ga S–type granite in the East Kunlun Orogen, Northern Tibetan Plateau: Implications for the Meso– to Neoproterozoic tectonic evolution. J. Asian Earth Sci. 130, 46–59.
He, D., Dong, Y., Liu, X., Zhou, X., Zhang, F., Sun, S., 2018. Zircon U–Pb geochronology and Hf isotope of granitoids in East Kunlun: implications for the Neoproterozoic magmatism of Qaidam Block, Northern Tibetan Plateau. Precambrian Res. 314, 377–393.
Hildreth, W., Moorbath, S., 1988. Crustal contributions to arc magmatism in the Andes of Central Chile. Contrib. Mineral. Petrol. 98, 455–489.
Hoskin, P.W.O., Schaltegger, U., 2003. The composition of zircon and igneous and metamorphic petrogenesis. Rev. Mineral. Geochem. 53, 27–55.
Hu, Z., Liu, Y., Gao, S., Liu, W., Zhang, W., Tong, X., Lin, L., Zong, K., Li, M., Chen, H., Zhou, L., Liu, L., 2012. Improved in situ Hf isotope ratio analysis of zircon using newly designed X skimmer cone and jet sample cone in combination with the addition of nitrogen by laser ablation multiple collector ICP-MS. J. Anal. At. Spectrom. 27, 1391–1399.
Hu, Y., Niu, Y., Li, J., Ye, L., Kong, J., Chen, S., Zhang, Y., Zhang, G., 2016. Petrogenesis and tectonic significance of the Late Triassic mafic dikes and felsic volcanic rocks in the East Kunlun Orogenic Belt, Northern Tibet Plateau. Lithos 245, 205–222.
Kay, R.W., 1978. Aleutian magnesian andesites: melts from subducted Pacific Ocean crust. J. Volcanol. Geotherm. Res. 4, 117–132.
Leake, B.E., Wooley, A.R., Arps, C.E.S., Birch, W.D., Gilbert, M.C., Grice, J.D., Hawthorne, F.C., Kato, A., Kisch, H.J., Krivovichev, V.G., 1997. Nomenclature of amphiboles: report of the subcommittee on amphiboles of the international mineralogical association, commission on new minerals and mineral names. Can. Mineral. 35, 219–246.
Lee, C.A., Cheng, X., Horodyskyj, U., 2006. The development and refinement of continental arcs by primary basaltic magmatism, garnet pyroxenite accumulation, basaltic recharge and delamination: insights from the Sierra Nevada, California. Contrib. Mineral. Petrol. 151, 222–242.
Li, R., Pei, X., Pei, L., Li, Z., Chen, G., Chen, Y., Liu, C., Wang, M., 2018. The Early Triassic Andean-type Halagatu granitoids pluton in the East Kunlun orogen, northern Tibet Plateau: Response to the northward subduction of the Paleo-Tethys Ocean. Gondwana Res. 62, 212–226.
Liu, C.D., Mo, X.X., Luo, Z.H., Yu, X.H., Chen, H.W., Li, S.W., Zhao, X., 2004. Mixing events between the crust-and mantle-derived magmas in Eastern Kunlun: evidence from zircon SHRIMP chronology. Chin. Sci. Bull. 49, 828–834.
Liu, Y.S., Zong, K.Q., Kelemen, P.B., Gao, S., 2008. Geochemistry and magmatic history of eclogites and ultramafic rocks from the Chinese continental scientific drill hole: subduction and ultrahigh-pressure metamorphism of lower crustal cumulates. Chem. Geol. 247, 133–153.
Liu, Y., Gao, S., Hu, Z., Gao, C., Zong, K., Wang, D., 2010. Continental and oceanic crust recycling-induced melt–peridotite interactions in the Trans-North China Orogen: U–Pb dating, Hf isotopes and trace elements in zircons from mantle xenoliths. J. Petrol. 51, 537–571.
Liu, B., Ma, C., Huang, J., Wang, L., Zhao, S., Yan, R., Sun, Y., Xiong, F., 2017. Petrogenesis and tectonic implications of Upper Triassic appinite dykes in the East Kunlun orogenic belt, northern Tibetan Plateau. Lithos 284-285, 766–778.
Ludwig, K.R., 2003. User's Manual for Isoplot/ex Version 3.00: A Geochronological Toolkit for Microsoft Excel. Berkeley Geochronology Center, Berkeley, CA Special Publication.
Ma, Q., Zheng, J., Griffin, W.L., Zhang, M., Tang, H., Su, Y., Ping, X., 2012. Triassic "adakitic" rocks in an extensional setting (North China): Melts from the cratonic lower crust. Lithos 149, 159–173.
Middlemost, E., 1994. Naming materials in the magma/igneous rock system. Earth Sci. Rev. 37, 215–224.
Mo, X.X., Luo, Z.H., Deng, J.F., Yu, X.H., Liu, C.D., Chen, H.W., Yuan, W.M., Liu, Y.H., 2007. Granitoids and crustal growth in the east-Kunlun orogenic belt. Geol. J. China Univ. 13, 403–414 (in Chinese with English abstract).
Moita, P., Santos, J.F., Pereira, M.F., Costa, M.M., Corfu, F., 2015. The quartz-dioritic Hospitais intrusion (SW Iberian Massif) and its mafic microgranular enclaves—evidence for mineral clustering. Lithos 224-225, 78–100.
Pearce, J.A., 2008. Geochemical fingerprinting of oceanic basalts with applications to ophiolite classification and the search for Archean oceanic crust. Lithos 100, 14–48.
Peccerillo, A., Taylor, S.R., 1976. Geochemistry of Eocene calc-alkaline volcanic rocks from the Kastamonu area, northern Turkey. Contrib. Mineral. Petrol. 58, 63–81.
Petford, N., Atherton, M., 1996. Na-rich partial melts from newly underplated Basaltic Crust: the Cordillera Blanca Batholith, Peru. J. Petrol. 37, 1491–1521.
Putirka, K.D., Mikaelian, H., Ryerson, F., Shaw, H., 2003. New clinopyroxene-liquid thermobarometers for mafic, evolved, and volatile-bearing lava compositions, with applications to lavas from Tibet and the Snake River Plain, Idaho. Am. Mineral. 88, 1542–1554.
Rapp, R.P., Shimizu, N., Norman, M.D., 2003. Growth of early continental crust by partial melting of eclogite. Nature 425, 605–609.
Ridolfi, F., Renzulli, A., 2011. Calcic amphiboles in calc-alkaline and alkaline magmas: thermobarometric and chemometric empirical equations valid up to 1,130 °C and 2.2 GPa. Contrib. Mineral. Petrol. 163, 877–895.
Ridolfi, F., Renzulli, A., Puerini, M., 2010. Stability and chemical equilibrium of amphibole in calc-alkaline magmas: an overview, new thermobarometric formulations and application to subduction-related volcanoes. Contrib. Mineral. Petrol. 160, 45–66.
Roger, F., Jolivet, M., Malavieille, J., 2008. Tectonic evolution of the Triassic fold belts of Tibet. Compt. Rendus Geosci. 340, 180–189.
Schiano, P., Monzier, M., Eissen, J.P., Martin, H., Koga, K.T., 2010. Simple mixing as the major control of the evolution of volcanic suites in the Ecuadorian Andes. Contrib. Mineral. Petrol. 160, 297–312.
Shao, F., Niu, Y., Liu, Y., Chen, S., Kong, J., Duan, M., 2017. Petrogenesis of Triassic granitoids in the East Kunlun Orogenic Belt, northern Tibetan Plateau and their tectonic implications. Lithos 282-283, 33–44.
Sisson, T.W., Grove, T.L., 1993. Temperatures and H_2O contents of low-MgO high-alumina basalts. Contrib. Mineral. Petrol. 113, 167–184.
Streck, M.J., 2008. Mineral textures and zoning as evidence for open system processes. Rev. Mineral. Geochem. 69, 595–622.
Sun, S.S., McDonough, W.F., 1989. Chemical and isotopic systematics of oceanic basalts: implications for mantle composition and processes. Geol. Soc. Lond. Spec. Publ. 42, 313–345.
Suzuki, Y., Nakada, S., 2007. Remobilization of highly crystalline felsic magma by injection of mafic magma: constraints from the middle sixth century eruption at Haruna volcano, Honshu, Japan. J. Petrol. 48, 1543–1567.
Tatsumi, Y., 2001. Geochemical modeling of partial melting of subducting sediments and subsequent melt-mantle interaction: Generation of high-Mg andesites in the Setouchi volcanic belt, Southwest Japan. Geology 29, 323–326.
Taylor, S.R., McLennan, S.M., 1985. The Continental Crust: Its Composition and Evolution. Blackwell Scientific Publications, Oxford, pp. 1–312.
Weidendorfer, D., Mattsson, H.B., Ulmer, P., 2014. Dynamics of magma mixing in partially crystallized magma chambers: textural and petrological constraints from the basal complex of the Austurhorn Intrusion (SE Iceland). J. Petrol. 55, 1865–1903.
Xia, R., Wang, C., Qing, M., Li, W., Carranza, E.J.M., Guo, X., Ge, L., Zeng, G., 2015. Zircon U–Pb dating, geochemistry and Sr–Nd–Pb–Hf–O isotopes for the Nan'getan granodiorites and mafic microgranular enclaves in the East Kunlun Orogen: record of closure of the Paleo-Tethys. Lithos 234-235, 47–60.
Xiong, F.H., Ma, C.Q., Zhang, J.Y., Liu, B., 2011. LA-ICP-MS zircon U-Pb dating, elements and Sr-Nd-Hf isotope geochemistry of the early Mesozoic mafic dyke swarms in Eastern Kunlun orogenic belt. Acta Petrol. Sin. 27, 3350–3364 (in Chinese with English abstract).
Xiong, F.H., Ma, C.Q., Zhang, J.Y., Liu, B., 2012. The origin of mafic microgranular enclaves and their host granodiorites from East Kunlun, Northern Qinghai-Tibet Plateau: implications for magma mixing during subduction of Paleo-Tethyan lithosphere. Mineral. Petrol. 104, 211–224.
Xiong, F.H., Ma, C.Q., Jiang, H.A., Liu, B., Zhang, J.Y., Zhou, Q., 2013. Petrogenetic and tectonic significance of Permian calc-alkaline lamprophyres, East Kunlun orogenic belt, Northern Qinghai-Tibet Plateau. Int. Geol. Rev. 55, 1817–1834.
Xiong, F.H., Ma, C.Q., Zhang, J.Y., Liu, B., Jiang, H.A., 2014. Reworking of old continental lithosphere: an important crustal evolution mechanism in orogenic belts, as evidenced by Triassic I-type granitoids in the East Kunlun orogen, Northern Tibetan Plateau. J. Geol. Soc. Lond. 171, 847–863.
Yang, J.S., Shi, R.D., Wu, C.L., Wang, X.B., Robinson, P., 2009. Dur'ngoi ophiolite in East Kunlun, Northeast Tibetan plateau: evidence for paleo-Tethyan suture in Northwest China. J. Earth Sci. 20, 303–331.
Yu, N., 2005. Characteristics of Metamorphic Rock Series and its Fluid Inclusions from Jinshuikou in Eastern Kunlun. Jilin University, Changchun, pp. 1–61 (M.A. Thesis, in Chinese with English abstract).
Zhang, J.Y., Ma, C.Q., Xiong, F.H., Liu, B., 2012. Petrogenesis and tectonic significance of the Late Permian-Middle Triassic calc-alkaline granites in the Balong region, eastern Kunlun Orogen, China. Geol. Mag. 149, 892–908.
Zhang, J., Ma, C., Li, J., Pan, Y., 2017. A possible genetic relationship between orogenic gold mineralization and post-collisional magmatism in the eastern Kunlun Orogen, western China. Ore Geol. Rev. 81, 342–357.